The Astrophysical Journal, 892:28 (23pp), 2020 March 20 https://doi.org/10.3847/1538-4357/ab737b

SN 2010kd: Photometric and Spectroscopic Analysis of a Slow-decaying Superluminous Supernova

Amit Kumar[1,2], Shashi Bhushan Pandey[1], Reka Konyves-Toth[3], Ryan Staten[4], Jozsef Vinko[3,5,6], J. Craig Wheeler[6], WeiKang Zheng[7], Alexei V. Filippenko[7,8], Robert Kehoe[4], Robert Quimby[9,10], Yuan Fang[11], Carl Akerlof[11], Tim A. McKay[11], Emmanouil Chatzopoulos[6,12], Benjamin P. Thomas[13], Govinda Dhungana[4], Amar Aryan[1,14], Raya Dastidar[1,15], Anjasha Gangopadhyay[1,2], Rahul Gupta[1,14], Kuntal Misra[1], Brajesh Kumar[1], Nameeta Brahme[2], and David Buckley[16]

[1] Aryabhatta Research Institute of Observational Sciences, Manora Peak, Nainital, 263002, India; amit@aries.res.in, shashi@aries.res.in
[2] School of Studies in Physics and Astrophysics, Pandit Ravishankar Shukla University, Chattisgarh 492010, India
[3] Konkoly Observatory, Research Center for Astronomy and Earth Sciences, Konkoly Thege M. ut 15-17, Budapest 1121, Hungary
[4] Department of Physics, Southern Methodist University, 3215 Daniel Avenue, Dallas, TX 75205, USA
[5] Department of Optics and Quantum Electronics, University of Szeged, Dom ter 9, Szeged 6720, Hungary
[6] Department of Astronomy, University of Texas, Austin, TX 79712, USA
[7] Department of Astronomy, University of California, Berkeley, CA 94720-3411, USA
[8] Miller Senior Fellow, Miller Institute for Basic Research in Science, University of California, Berleley, CA 94720, USA
[9] Department of Astronomy/Mount Laguna Observatory, San Diego State University, 5500 Campanile Drive, San Diego, CA 92812-1221, USA
[10] Kavli IPMU (WPI), UTIAS, The University of Tokyo, Kashiwa, Chiba 277-8583, Japan
[11] Department of Physics, University of Michigan, 450 Church Street, Ann Arbor, MI 48109-1040, USA
[12] Department of Physics & Astronomy, Louisiana State University, Baton Rouge, LA 70803, USA
[13] Department of Astronomy, University of Texas at Austin, Austin, TX, USA
[14] Department of Physics, Deen Dayal Upadhyaya Gorakhpur University, Gorakhpur 273009, India
[15] Department of Physics & Astrophysics, University of Delhi, Delhi-110 007, India
[16] South African Astronomical Observatory, P.O. Box 9, Observatory 7935, Cape Town, South Africa

Received 2019 November 21; revised 2020 February 4; accepted 2020 February 5; published 2020 March 23

Abstract

This paper presents data and analysis of SN 2010kd, a low-redshift ($z = 0.101$) H-deficient superluminous supernova (SLSN), based on ultraviolet/optical photometry and optical spectroscopy spanning between −28 and +194 days relative to *B*-band maximum light. The *B*-band light-curve comparison of SN 2010kd with a subset of well-studied SLSNe I at comparable redshifts indicates that it is a slow-decaying PTF12dam-like SLSN. Analytical light-curve modeling using the `Minim` code suggests that the bolometric light curve of SN 2010kd favors circumstellar matter interaction for the powering mechanism. `SYNAPPS` modeling of the early-phase spectra does not identify broad H or He lines, whereas the photospheric-phase spectra are dominated by O I, O II, C II, C IV, and Si II, in particular the presence of both low- and high-velocity components of O II and Si II lines. The nebular-phase spectra of SN 2010kd are dominated by O I and Ca II emission lines similar to those seen in other SLSNe I. The line velocities in SN 2010kd exhibit flatter evolution curves similar to SN 2015bn but with comparatively higher values. SN 2010kd shows a higher single-zone local thermodynamic equilibrium temperature in comparison to PTF12dam and SN 2015bn, and it has an upper O I ejected mass limit of $\sim 10\,M_\odot$. The host of SN 2010kd is a dwarf galaxy with a high star formation rate ($\sim 0.18 \pm 0.04\,M_\odot\,\mathrm{yr}^{-1}$) and extreme emission lines.

Unified Astronomy Thesaurus concepts: Supernovae (1668); Core-collapse supernovae (304); Photometry (1234); Spectroscopy (1558)

1. Introduction

Superluminous supernovae (SLSNe) are the most luminous SNe, having a mean absolute magnitude of ∼−21.7 mag (Gal-Yam 2012; Quimby et al. 2013; Nicholl et al. 2016b; De Cia et al. 2018; Angus et al. 2019; Inserra 2019). SLSNe are very rare, comprising only ∼0.01% of the normal population of core-collapse SNe (CCSNe; Quimby et al. 2013; McCrum et al. 2015; Prajs et al. 2017). The era of SLSN studies started with the discovery of SN 2005ap (Quimby et al. 2007) by the Robotic Optical Transient Search Experiment (ROTSE; Akerlof et al. 2003). Later, new sky surveys came into existence and began discovering SLSNe at a rate of ∼3 per month; see, for example, the Palomar Transient Factory (PTF; Quimby et al. 2011), Pan-STARRS1 (PS1; Chornock et al. 2013), and the Zwicky Transient Facility (ZTF; Lunnan et al. 2018). Being highly luminous, SLSNe can be used to reveal and understand the last evolutionary phases of very massive stars and to probe the high-redshift universe. The host galaxies of SLSNe are usually faint dwarf galaxies having low metallicity, with extremely strong emission lines suggesting enhanced star-forming activity (Lunnan et al. 2014; Leloudas et al. 2015; Perley et al. 2016; Chen et al. 2017b; Schulze et al. 2018).

Like normal SNe, SLSNe are spectroscopically divided into two categories: hydrogen-poor (SLSNe I) and hydrogen-rich (SLSNe II; Gal-Yam 2012). SLSNe I are thought to be a subtype of SNe Ic, because after a few weeks, they exhibit spectral features similar to those of SNe Ic (Pastorello et al. 2010; Inserra et al. 2013). SLSNe I are broadly classified into fast- and slow-decaying categories (Quimby et al. 2011, 2018; Inserra et al. 2017; Inserra 2019); however, they seem to have a wider range of postpeak decay rates with no significant gap (Nicholl et al. 2015a; De Cia et al. 2018).

SLSNe are among one of the least understood SNe because not only are their underlying progenitors unclear, but their extremely high peak luminosity is also unexplained using conventional SN power-source models (Gal-Yam 2012). Various studies have suggested different power sources for SLSNe I (Moriya et al. 2018; Wang et al. 2019). To explain the required high peak luminosity of SLSNe I with the primary power source being the radioactive decay (RD) of ^{56}Ni → ^{56}Co → ^{56}Fe, the synthesized ^{56}Ni mass ($M_{\rm Ni}$) should be $\gtrsim 5\,M_\odot$ (Gal-Yam 2012); however, the synthesized $M_{\rm Ni}$ in CCSNe cannot exceed $\sim 4\,M_\odot$ (Umeda & Nomoto 2008). Moreover, late-time observations of SLSNe I suggest that $M_{\rm Ni} \lesssim 1\,M_\odot$ for many SLSNe I (Pastorello et al. 2010; Chen et al. 2013), inconsistent with the $M_{\rm Ni}$ estimated by the RD model. Also, the median of the observed ejecta masses ($M_{\rm ej}$) calculated using a sample of SLSNe I is $\sim 6\,M_\odot$ (Nicholl et al. 2015a). This value is closer to (or sometimes even lower than) the $M_{\rm Ni}$ obtained from the RD model, which makes this model unphysical. The pair-instability SN (PISN) model was also suggested as a power mechanism for some slow-decaying SLSNe I (e.g., SN 2007bi; Gal-Yam et al. 2009), but later it was found that the bluer color and the fast-rising rate of slow-decaying SLSNe I contradict the PISN model (Kasen et al. 2011; Dessart et al. 2012; Nicholl et al. 2013; Jerkstrand et al. 2017).

Spin-down millisecond magnetars having magnetic fields of a few $\times 10^{14}$ G are also considered as possible power sources for many SLSNe I (Kasen & Bildsten 2010; Woosley 2010; Inserra et al. 2013; Dessart 2019). In addition, a subset of SNe Ib/c and some gamma-ray bursts (GRBs) may have magnetars as central power sources (Wheeler et al. 2000; Metzger et al. 2011). However, contrary to this, many SLSNe I have prepeak bumps (e.g., LSQ14bdq; Nicholl et al. 2015b) and postpeak undulations (e.g., SN 2015bn; Nicholl et al. 2015a) in their light curves that cannot be explained well using a spin-down magnetar (MAG) model.

The circumstellar matter interaction (CSMI) is also suggested as a possible powering mechanism for many SLSNe I (Chevalier & Irwin 2011). Recently, Wheeler et al. (2017) found that SN 2017egm showed an irregular light curve with a convex rise to peak, which is inexplicable by either the MAG or RD models. Both of these models demand a concave downward rise and decline from the peak, so SN 2017egm proved to be powered by the CSMI. Conversely, SLSNe I do not show any signatures of CSM interaction in their spectra, except for iPTF13ehe (Yan et al. 2015), iPTF15esb, and iPTF16bad (Yan et al. 2017a). In many cases, light-curve fitting of SLSNe I requires a combination of the above models; we call these "HYBRID" models based on Chatzopoulos et al. (2012). For example, the primary power source may be a central engine, but a small amount of CSMI might also play role (Chen et al. 2017a; Inserra et al. 2017).

In this paper, we present the analysis of the optical photometric and spectroscopic data of the nearby SN 2010kd. For the photometric study, early-time ROTSE-IIIb discovery data along with multiband *Swift*-UVOT data and other published optical photometry taken from Roy (2012) in the Johnson *UBV* and Cousins *RI* filters are used. The spectral data for SN 2010kd were obtained using the 9.2 m Hobby–Eberly Telescope (HET-9.2m) and the Keck I 10 m telescope (Keck-10m).

Section 2 discusses the multiband light-curve analysis and analytical fitting to the bolometric light curve using `MINIM`. The optical light-curve comparison of SN 2010kd with some well-studied SLSNe I at comparable redshift is presented in Section 3. Section 4 describes the spectroscopic study of SN 2010kd along with the `SYNAPPS` spectral modeling of the photospheric-phase spectra. In Section 5, we compare spectra of SN 2010kd with those of some slow- and fast-decaying SLSNe I and several SNe Ic-BL. Section 6 presents a velocity comparison of various identified elements of SN 2010kd with a set of well-studied SLSNe I at comparable redshift. In Section 7, we determine various physical parameters of line luminosities during the nebular phase, their ratios, and comparison with a set of SLSNe I. Constraints on the host-galaxy properties are discussed in Section 8. We summarize results in Section 9. Throughout this paper, the temporal phase is referred with respect to the *B*-band maximum light and the magnitudes are expressed in Vega. The phase before *B*-band maximum is considered to be the hot photospheric phase; after maximum, it is termed as the cool photospheric phase and after +90 days designated as the nebular phase (Gal-Yam 2019).

2. ROTSE-IIIb Discovery and Photometry

On 2010 November 14 (UT dates are used throughout this paper), SN 2010kd was discovered by the ROTSE-IIIb telescope as part of the ROTSE Supernova Verification Project (RSVP) at an apparent magnitude of ∼17.2 mag (Vinko et al. 2010). SN 2010kd was discovered in a faint and metal-poor dwarf galaxy at J2000 coordinates $\alpha = 12^{\rm h}08^{\rm m}01\overset{\rm s}{.}11$ and $\delta = +49^\circ 13' 31\overset{\prime\prime}{.}1$.

The first optical spectrum of SN 2010kd was observed using the HET-9.2 m on 2010 November 22, showing a narrow Hα emission line from the host galaxy at redshift $z \approx 0.1$. There were no broad H or He features, but spectral modeling with the code `SYNAPPS` (Thomas et al. 2011) recognized an enrichment of carbon and oxygen lines (Vinko et al. 2010, 2012). From follow-up photometry with ROTSE-IIIb, the peak absolute magnitude of SN 2010kd in the clear filter was constrained to be ~ -21.4 mag. The luminous peak absolute magnitude and the presence of O II features at shorter wavelengths in the spectrum placed SN 2010kd in the category of SLSNe I. Multiwavelength follow-up observations were triggered with *Swift*-UVOT and XRT. *Swift*-UVOT detected SN 2010kd as a strong ultraviolet (UV) source. Even though no significant X-ray emission was detected, stacked observations gave an upper limit of $\sim 0.8 \times 10^{42}$ erg s^{-1} (see the upper-left panel of Figure 2).

We constrained the explosion date to be ${\rm MJD}_{\rm expl} \approx 55{,}483.09 \pm 0.90$ by extrapolating the premaximum light curve down to the brightness level of the host galaxy ($m_u = +21.54 \pm 0.23$ mag; see Section 8 for details) using a third-order spline function fit to the prepeak UV data. This calculated ${\rm MJD}_{\rm expl}$ is in good agreement with that estimated by Chatzopoulos et al. (2013). Throughout the present analysis, data of SN 2010kd were corrected for Galactic extinction, $E(B-V) = 0.02$ mag, using dust maps published by Schlegel et al. (1998); however, the host-galaxy extinction, $E(B-V) = 0.15$ mag, was adopted from Schulze et al. (2018). Throughout the paper, data have also been corrected for cosmological expansion; see Equation (1).

2.1. Optical Light-curve Analysis of SN 2010kd

In Figure 1, *Swift*-UVOT photometry (*UVW2*, *UVM2*, *UVW1*, *u*, *b*, and *v* filters), ROTSE-IIIb photometry in the clear filter, and the *B*-band data taken from Roy (2012) are presented. Owing to the good temporal coverage of *Swift*-UVOT early-time data, the epoch of peak brightness could be

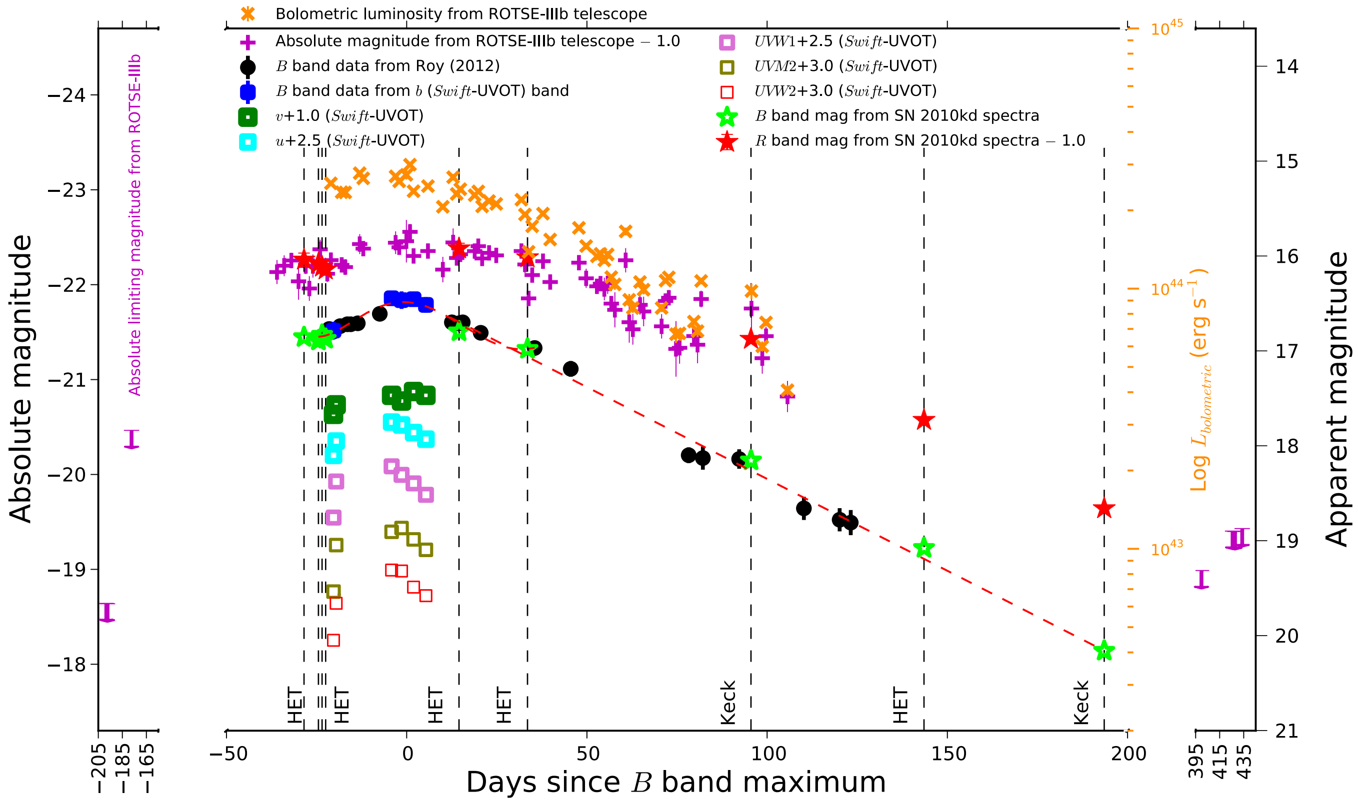

Figure 1. Multiband light curves of SN 2010kd, including the ROTSE-IIIb discovery photometric data in the clear filter (magenta plus signs) along with *Swift*-UVOT data (squares of different colors), are plotted. The Johnson *B*-band photometry (in black) was taken from Roy (2012). The magenta arrows represent upper limits obtained by the ROTSE-IIIb at prediscovery and very late epochs. The *B*- and *R*-band magnitudes calculated from spectra of SN 2010kd using the `sms` (Inserra et al. 2018c) code are plotted with star symbols (lime and red, respectively). Around peak brightness, the M_B light curve is fitted with a third-order spline function to get the $M_{B,\rm peak}$ and the corresponding $\mathrm{MJD}_{B,\rm peak}$. The postpeak (from peak to +194 days) data points are fitted using a straight line (in red dashed) to estimate the postpeak decay rate. Vertical dashed black lines represent epochs of spectral observations used in the present analysis. The bolometric light curve calculated from ROTSE-IIIb discovery photometry is plotted in orange cross signs, showing a peak at $\sim(2.67 \pm 0.20) \times 10^{44}$ erg s^{-1} (ROTSE-IIIb photometry data is published electronically).

tightly constrained in various bands. In Figure 1, we can see that the light-curve peak comes earlier in the UV bands and at later epochs in redder bands, as is typical of CCSNe (Taddia et al. 2018). We derived absolute magnitudes from the extinction-corrected apparent magnitudes using the formula[17]

$$M = m - 5\log(d_L^{17}/10\ \mathrm{pc}) + 2.5\log(1+z) \qquad (1)$$

(Hogg et al. 2002; Lunnan et al. 2016). To precisely derive the *B*-band peak brightness, *Swift*-UVOT *b*-band data were converted to Johnson *B* using the transformation equations given by Poole et al. (2008). To constrain the late-time photometry (up to +194 days), the *B*- and *R*-band magnitudes were calculated from the late-time spectra using the `sms` (Inserra et al. 2018c) code. The derived values of synthetic spectral magnitudes and those estimated from the imaging are in good agreement (with a scatter $\lesssim$0.15 mag). The *B*-band maximum date ($\mathrm{MJD}_{B,\rm peak} = 55,550.48$) and the corresponding peak absolute magnitude ($M_{B,\rm peak} = -21.80 \pm 0.02$ mag) were calculated by fitting a third-order spline function to the *B*-band absolute magnitude (M_B) light curve around maximum brightness (−20 to +20 days; red dashed line). The estimated value of the $M_{B,\rm peak}$ of SN 2010kd is consistent with the mean peak absolute magnitudes of the sample of SLSNe I published by Quimby et al. (2013), Nicholl et al. (2016b), and Inserra et al. (2018a).

The postpeak light curve (from peak to +194 days) can be fitted well with a single straight line (in mag; thus, exponential in flux) having a decay rate of ∼0.019 mag day^{-1}, which is shallower than the $^{56}\mathrm{Ni} \rightarrow {}^{56}\mathrm{Co}$ decay rate (0.11 mag day^{-1}) but steeper than that predicted for the $^{56}\mathrm{Co} \rightarrow {}^{56}\mathrm{Fe}$ decay rate (0.0098 mag day^{-1}). The M_B light curve decayed by 1 mag from the peak value in ∼56 days, and the time taken to decay to the half-flux from the peak-flux value is ∼45 days. Compared with the PTF sample of SLSNe I (De Cia et al. 2018), the postpeak decay rate of SN 2010kd is shallower than the average (0.04 mag day^{-1}) value of the early-time decline ($\lesssim$+60 days) but steeper than the average value (∼0.01 mag day^{-1}) of the late-time decline ($\gtrsim$+60 days).

2.2. Pseudobolometric Light Curve Using ROTSE-IIIb

ROTSE-IIIb absolute magnitudes cover a temporal phase of −35 to +105 days, showing a clear filter peak absolute magnitude ∼−21.4 mag; see Figure 1. To obtain a pseudobolometric light curve with ROTSE-IIIb unfiltered broadband photometry, we first perform a calibration using *UBVRI* photometry from Roy (2012). Although there is no infrared (IR) photometry of SN 2010kd, a second calibration to *UBVRIJHK* is performed by applying a correction from ROTSE-IIIb photometry to *UBVRIJHK* for SN 2007gr (Bianco et al. 2014), another SN Ic with extensive data in the UV through IR bands. For SN 2007gr, a linear interpolation is used to incorporate the flux between the *I* and *J*, *J* and *H*, and *H* and

---

[17] The luminosity distance.

K filters. Although this is an approximation for the flux from SN 2010kd over IR wavelengths, a pseudobolometric light curve is established from −22 to +105 days.

Owing to the fact that ROTSE-IIIb uses an open CCD with broad transmission covering 3000–10,000 Å, we first establish a calibration relation with *UBVRI* photometry. Common epochs are derived by interpolating *UBVRI* data sets to ROTSE-IIIb data. To obtain the flux, we calibrate ROTSE-IIIb magnitudes to R-band magnitudes, correct for the extinction using values of $E(B-V)=0.17$ mag, and use the Johnson–Cousins photometric system as described by Bessell (1990). Following the methodology of Dhungana et al. (2016), a linear correlation is seen between the ratio of $L_{\rm ROTSE}$ and $L_{\rm UBVRI}$ to the $(B-V)$ color. This linear relationship is then used to calibrate $L_{\rm ROTSE}$ to $L_{\rm UBVRI}$, establishing a pseudobolometric light curve with peak luminosity $\sim(2.26\pm0.11)\times10^{44}\,{\rm erg\,s^{-1}}$. The rms of the residuals in fitting the $(B-V)$ dependence of $L_{\rm ROTSE}/L_{\rm UBVRI}$ yields 8% precision.

The same process is performed for SN 2007gr using publicly available $UBVr'i'$ data from the Fred L. Whipple Observatory (FLWO) on Mount Hopkins in Arizona (Bianco et al. 2014), similarly establishing a calibration with 7% precision. To obtain the flux for this object, the Johnson system is used for the *UBV* filters and the Sloan Digital Sky Survey (SDSS) photometric system (Fukugita et al. 1996) is used for the $r'i'$ filters. Integrated luminosity is calculated by adopting a distance of 10.6 Mpc (Chen et al. 2014). Once ROTSE-IIIb is calibrated to *UBVRI*, a second calibration from ROTSE-IIIb to *UBVRIJHK* is performed by fitting the ratio of $L_{\rm UBVRI}$ and $L_{\rm UBVRIJHK}$ to the $(B-V)$ color and applying this to $L_{\rm ROTSE}$. The FLWO sample also contains *JHK* data, where the Two Micron All Sky Survey system (Cohen et al. 2003) is used to obtain the flux for these filters. The rms of the residuals for this calibration yields 6% precision. In order to incorporate unobserved flux between the I and J, J and H, and H and K filters, a similar calibration is performed, this time fitting the ratio of $L_{\rm UBVRIJHK}$ to $L_{\rm UBVRIJHK}$ including unobserved flux between filters versus the $(B-V)$ color. To calculate this additional flux at each epoch, a linear interpolation between the fluxes seen in each filter is used. Finally, the resulting fit is applied to $L_{\rm ROTSE}$ for SN 2010kd, increasing the peak luminosity to $\sim(2.67\pm0.20)\times10^{44}\,{\rm erg\,s^{-1}}$, as seen in Figure 1.

2.3. Bolometric Light Curve and Model Fitting Using `Minim`

Bolometric light curve of the SN 2010kd was calculated using a Python-based code `Superbol` (Nicholl 2018). To get data near the peak brightness, we converted *Swift*-UVOT u, b, and v magnitudes to Johnson U, B, and V magnitudes, respectively, using the transformation equations given by Poole et al. (2008). The R and I light curves are interpolated using third-order polynomial fits to a common set of observed epochs with respect to observations in the B band. However, we assume a constant color to extrapolate late-time UVW2, UVM2, UVW1, and U-band data. We further extrapolate the blackbody (BB) spectral energy distribution (SED) by integrating the observed UV-optical flux to estimate the expected flux values in the near-infrared (NIR) region. The data were also corrected for Galactic as well as host extinction. The flux and wavelength of individual bands are shifted to the rest frame. The full bolometric light curve covers phases from −20 to +123 days and shows a peak luminosity of $\sim(2.51\pm0.10)\times10^{44}\,{\rm erg\,s^{-1}}$ (see upper-left panel of Figure 2). It is notable that the peak bolometric luminosity calculated using the method described in Section 2.2 from ROTSE-IIIb data and that derived with `Superbol` for multiband data are in good agreement within the uncertainties.

We used the code `Minim` (Chatzopoulos et al. 2013) to fit various models to the bolometric light curve of SN 2010kd. `Minim` is a χ^2-minimization code which utilizes Price algorithm (Brachetti et al. 1997), a controlled random search technique, briefly discussed by Chatzopoulos et al. (2013). Semianalytic light-curve models—RD, MAG, HYBRID (constant density CSMI + RD), HYBRIDW (wind-like CSMI + RD), and HYBRIDW only with CSMI contribution (CSMI-only) models—were fitted to the bolometric light curve of SN 2010kd (see Figure 2). The electron-scattering opacity (κ) may vary from ∼0.1 to 0.2 $\rm cm^2\ g^{-1}$ for half- and fully ionized materials, respectively (Nicholl et al. 2015a). We choose $\kappa=0.1\ {\rm cm^2\ g^{-1}}$, considering that in the case of H-poor SLSNe I species like oxygen, carbon, and iron are roughly half ionized, as adopted by Inserra et al. (2013). So, HYBRID, HYBRIDW, and CSMI-only models are fitted with $\kappa=0.1\ {\rm cm^2\ g^{-1}}$.

All of the calculated parameters for the RD, MAG, HYBRID, HYBRIDW, and CSMI-only models are, respectively, listed in Tables 1–5. Values of $M_{\rm ej}$ are calculated using Equation (3) from Chatzopoulos et al. (2013), both for the RD and the MAG models.

Statistically, all the models reproduced the bolometric light curve of SN 2010kd within the error bars, as can be inferred from the respective values of χ^2 per degree of freedom (DOF). But, the value of $M_{\rm Ni}$ given by the RD model is higher than the estimated $M_{\rm ej}$ value, which is unphysical; this indicates that the RD of ^{56}Ni cannot be considered as a primary power source of SN 2010kd. In comparison to other discussed models, the MAG model reproduced the bolometric light curve of SN 2010kd with a higher value of χ^2/DOF (0.95). However, the parameters of SN 2010kd estimated by the MAG model are in good agreement with the values suggested for PTF12dam (Nicholl et al. 2013) and SN 2015bn (Nicholl et al. 2016b); see Table 2.

The HYBRID and HYBRIDW models reproduced the bolometric light curve of SN 2010kd with $\chi^2/{\rm DOF}=0.76$ and 0.56, respectively. In the lower-right panel of Figure 2, we also plot the HYBRIDW model with only a CSMI contribution by setting $M_{\rm Ni}=0.0\,M_\odot$ (CSMI-only model). The CSMI-only model has also been able to reproduce the bolometric light curve with the comparatively lower value of $\chi^2/{\rm DOF}=0.55$, which might indicate that ^{56}Ni heating does not play a significant role in the HYBRIDW (CSMI+RD) model.

With the lowest value of χ^2/DOF (0.55), the CSMI-only model constrains $M_{\rm ej}\approx18.47\pm0.65\,M_\odot$, $M_{\rm csm}\approx22.68\pm0.53\,M_\odot$, and explosion ejecta velocity $\sim(24.75\pm0.11)\times10^3\,{\rm km\,s^{-1}}$. The estimated $M_{\rm ej}$ value for SN 2010kd is higher in comparison to the median of the observed $M_{\rm ej}$ ($\sim6\,M_\odot$) calculated using a sample of SLSNe I (Nicholl et al. 2015a) and a sample of SNe IIb, Ib, and Ic ($\lesssim4.4\pm1.3\,M_\odot$; Wheeler et al. 2015). The parameters for SN 2010kd obtained using the best-fit CSMI-only model are given in Table 5. In summary, based on our model fitting, the CSMI or spin-down millisecond magnetar might be the possible powering mechanism for SN 2010kd.

Along with the best-fit bolometric light curve, the limiting X-ray luminosity ($\lesssim0.8\times10^{42}\ {\rm erg\,s^{-1}}$) calculated using the

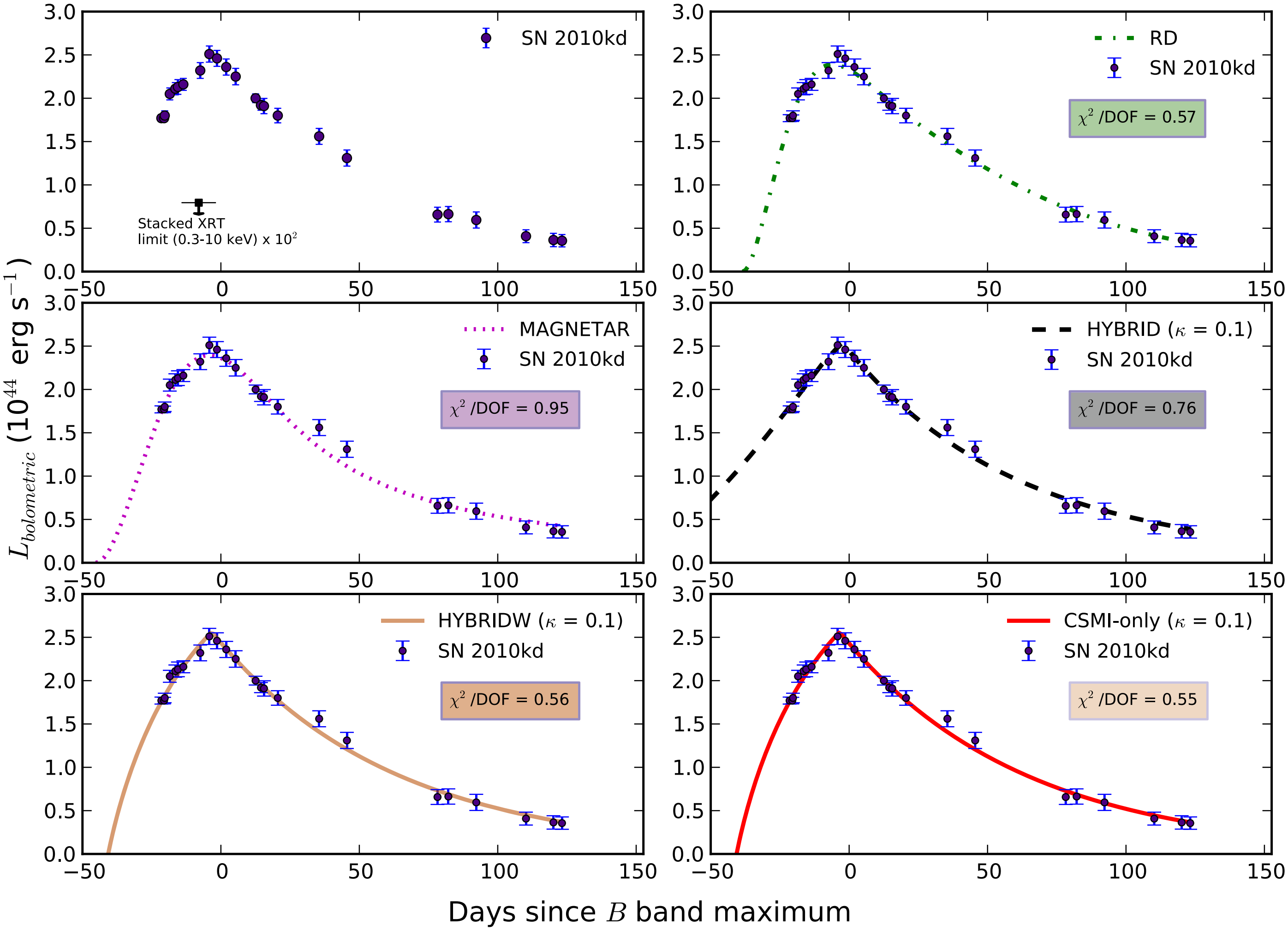

Figure 2. In the upper-left panel, we plot the bolometric light curve of SN 2010kd, whereas the semianalytic light-curve models (RD, MAG, HYBRID, HYBRIDW, and CSMI-only) fitted to the bolometric light curve of SN 2010kd using `Minim` (Chatzopoulos et al. 2013) are shown in five different panels. The photometric data points of SN 2010kd are shown in blue whereas the five modeled light curves are color coded with the best-fit model (HYBRIDW/CSMI-only) shown in red. The HYBRID, HYBRIDW, and CSMI-only models are fitted with $\kappa = 0.1$ cm^2 g^{-1}. In the upper-left panel, the limiting XRT luminosity using stacked data (described in Appendix A.3) is also shown with the black arrow.

stacked images obtained from *Swift*-XRT is also plotted (upper-left panel of Figure 2, black arrow); data reduction is discussed in Appendix A.3. SN 2010kd is not visible in X-rays even near peak optical brightness, as seen in other XRT-observed SLSNe I except for PTF12dam (which was detected; Margutti et al. 2018).

3. Photometric Comparison of SN 2010kd with Other SLSNe I

For the present study, the following two broad criteria were adopted to build the sample of SLSNe I listed in Table 6:

(1) The value of the redshift should be within ±0.05 relative to the redshift of SN 2010kd.

(2) The object should have photometric data in at least four bands (*BVRI* or *griz*).

For consistency, throughout this work the distances are calculated using the cosmological parameters $H_0 = 67.8 \pm 0.9$ km s^{-1} Mpc^{-1}, $\Omega_m = 0.308 \pm 0.012$, and $\Omega_\lambda = 0.692$ (Planck Collaboration XIII et al. 2016). Except for Gaia16apd (Kangas et al. 2017), the host-galaxy extinction values for all the tabulated SLSNe I are taken from Schulze et al. (2018), which were estimated using SED modeling. The $M_{B,\mathrm{peak}}$ and corresponding MJD$_{B,\mathrm{peak}}$ presented in Table 6 are calculated independently for all the tabulated SLSNe I. SN 2007bi does not have *B*-band magnitudes around the peak brightness, so MJD$_{R,\mathrm{peak}}$ is taken in place of MJD$_{B,\mathrm{peak}}$.

We can subdivide our sample of seven comparison SLSNe I into fast-, slow-, and intermediate-decaying SLSNe I based on postpeak decay rates. PTF10hgi, SN 2011ke (Inserra et al. 2013), and SSS120810:231802–560926 (Nicholl et al. 2014) are designated as fast-decaying SLSNe I, having postpeak decay rates close to that of ^{56}Ni → ^{56}Co. On the other hand, SN 2007bi (Gal-Yam et al. 2009), PTF12dam (Nicholl et al. 2013), and SN 2015bn (Nicholl et al. 2016b) are slow-decaying SLSNe I, having a postpeak decay rate close to that of ^{56}Co → ^{56}Fe. Photometrically, Gaia16apd resembles an intermediate (between slow- and fast-decaying) SLSN, while its late-time spectroscopic features are similar to those of PTF12dam (Kangas et al. 2017). However, this division between fast and slow-decaying SLSNe I is not broadly accepted for a larger sample of SLSNe I (Nicholl et al. 2017; De Cia et al. 2018; Lunnan et al. 2018).

Table 1
Best-fit Parameters for the RD Model

$M_{\rm Ni}$ [a] ($M_\odot$)	t_d [b] (days)	A_γ [c]	$M_{\rm ej}$ [d] (for $\kappa = 0.1$ cm^2 g^{-1}) ($M_\odot$)	χ^2/DOF
20.3 ± 0.16	20.3 ± 0.16	179.9 ± 7.73	4.26 ± 0.13	0.57

Notes.
[a] $M_{\rm Ni}$: radioactive ^{56}Ni synthesized mass (in $M_\odot$).
[b] t_d: effective diffusion timescale (in days).
[c] A_γ: optical depth for the gamma-rays measured after 10 days of explosion.
[d] $M_{\rm ej}$: ejecta mass (in $M_\odot$).

3.1. *B-band Light-curve Comparison of SN 2010kd with Other SLSNe I*

In this section, we compare the M_B light curve of SN 2010kd with the light curves of seven SLSNe I given in Table 6 (see Figure 3). The light curves of all the plotted SLSNe I are corrected for Galactic as well as host extinction. For those events having data in SDSS filters (SN 2011ke, PTF12dam, and SN 2015bn), the *g*- and *r*-band data were transformed to the *B* band using the transformation equations given by Jordi et al. (2006). To trace the evolution, the M_B light curves of all the plotted SLSNe I are fitted with a high-order spline function, shown with solid lines of different colors. SN 2010kd seems to have an $M_{B,\rm peak}$ value close to that seen in the case of PTF12dam and Gaia16apd. However, the $M_{B,\rm peak}$ value of SN 2010kd seems lower than that observed in the case of SN 2015bn but larger than that observed for PTF10hgi, SN 2011ke, and SSS120810:231802–560926 (slow-decliners), as shown in the inset panel on the left side of Figure 3. This illustrates that SN 2010kd is one of the luminous SLSNe I.

Fast-decaying SLSNe I (PTF10hgi, SN 2011ke, and SSS120810:231802–560926) have decay rates of ~0.06 mag day^{-1}, slow-decaying SLSNe I (SN 2007bi, PTF12dam, and SN 2015bn) show decay rates of ~0.02 mag day^{-1}, and Gaia16apd has a decay rate of ~0.045 mag day^{-1}. SN 2010kd has a decay rate of ~0.019 mag day^{-1}, similar to those estimated for slow-decaying SLSNe I, especially matching with the decay pattern shown by PTF12dam, as shown in the inset panel on the right side of Figure 3. SN 2010kd seems to have a slow rising rate similar to SN 2015bn. All fast-decaying SLSNe I in the present sample exhibit a decay rate slightly shallower than $^{56}\mathrm{Ni} \rightarrow {}^{56}\mathrm{Co}$; however, all slow-decaying SLSNe I of the sample exhibit a slightly steeper decay than that predicted for $^{56}\mathrm{Co} \rightarrow {}^{56}\mathrm{Fe}$. In summary, the *B*-band absolute magnitude light-curve evolution of SN 2010kd is similar to that of slow-decaying SLSNe I, and in particular closer to PTF12dam.

3.2. *Color Evolution Comparison of SN 2010kd with Other SLSNe I*

Optical through NIR colors of SLSNe I are useful probes for understanding the temperature evolution during the photospheric phase. The optical color evolution of SN 2010kd is plotted in Figure 4. From ~−20 to +15 days, all plotted color curves of SN 2010kd do not show significant change, indicating nearly constant temperatures around the time of peak brightness. After ~+15 days, these color curves of SN 2010kd evolve redder, which can be associated with a decrease in the photospheric temperature as the SN dims during the postmaximum phases.

Figure 5 illustrates the evolution of the observed $(U - B)$ and $(B - V)$ color curves of SN 2010kd in comparison to SLSNe I listed in Table 6. Only the $(U - B)$ and $(B - V)$ colors are compared because $(V - R)$ and $(R - I)$ seem to evolve very similarly to $(B - V)$. Color curves of all the plotted SLSNe I are corrected for the Galactic as well as host-galaxy extinction, and to trace the evolution, the color curves are fitted with a high-order spline function. For comparison, the SDSS $(u - g)$ and $(g - r)$ colors of PTF10hgi, SN 2011ke, PTF12dam and SN 2015bn were transformed to Johnson $(U - B)$ and $(B - V)$ colors, using the transformation equations and uncertainties given by Jordi et al. (2006).

The $(B - V)$, $(V - R)$, and $(R - I)$ color curves appear to have nearly similar evolution, starting from ~0 (at −20 days) to ~+0.4 mag (at +123 days), indicating slow cooling and expansion of the SN envelope. In the same time regime, the $(U - B)$ color comparatively becomes redder (~−0.9 to −0.2 mag) sharply. This could be explained partly by cooling due to expansion and partly because of the enhancement of metallic (mostly Fe II) features in the UV. Color curves of SN 2010kd show that it is very blue at early epochs (from +15 to ~+90 days) and undergoes faster cooling in the *U* band compared with other optical bands.

The $(B - V)$ color evolution of fast-decaying (PTF10hgi, SN 2011ke, and SSS120810:231802–560926) SLSNe I appears to become redder faster in comparison to slow decliners (SN 2007bi, PTF12dam, and SN 2015bn); see the upper panel of Figure 5. It is also clear that for slow-decaying SLSNe I, the $(B - V)$ color becomes redder slowly until ~100 days after peak brightness, and at later epochs, it becomes constant around ~0.3 mag (except SN 2015bn, which shows negative color values). In contrast, the $(B - V)$ colors of fast-decaying SLSNe I become redder continuously up to ~1.5 mag (at ~100 days). The $(B - V)$ color evolution of Gaia16apd appears similar to the fast-decaying SLSNe I. SN 2010kd seems to have a similar $(B - V)$ color curve to SN 2007bi and PTF12dam.

In the case of $(U - B)$ color comparison, SN 2007bi does not have data in the *U* band, so the remaining six SLSNe I are chosen for comparison (see Figure 5, lower panel). Similar to $(B - V)$, the $(U - B)$ color evolution of the fast-decaying SLSNe I turns redder sharply in comparison to the slow-decaying SLSNe I. The $(U - B)$ color evolution of SN 2010kd seems similar to those seen in the case of Gaia16apd and SN 2015bn.

4. Spectroscopic Observations of SN 2010kd

As part of the present analysis, spectra of SN 2010kd were acquired using the Marcario Low-Resolution Spectrograph (LRS; Hill et al. 1998) on the HET-9.2 m and the Low-Resolution

Table 2
Best-fit Parameters for the MAG Model

R_0[a] (10^{13} cm)	E_p[b] (10^{51} erg)	t_d[c] (days)	t_p[d] (days)	$v_{\rm exp}$[e] (10^3 km s^{-1})	$M_{\rm ej}$[c] (for $\kappa = 0.1$ cm^2 s^{-1}) ($M_\odot$)	P_i[f] (ms)	B[g] (10^{14} G)	χ^2/DOF
1.0 ± 1.25	3.37 ± 0.06	35.0 ± 0.88	46.85 ± 2.08	11.2 ± 0.98	5.71 ± 0.285	2.44 ± 0.13	0.78 ± 0.005	0.95

Notes.
[a] R_0: progenitor radius (in 10^{13} cm).
[b] E_p: magnetar rotational energy (in 10^{51} erg).
[c] discussed above.
[d] t_p: magnetar spin-down timescale (in days).
[e] $v_{\rm exp}$: SN expansion velocity (in 10^3 km s^{-1}).
[f] P_i: initial period of the magnetar (in ms).
[g] B: magnetic field of the magnetar (10^{14} G).

Table 3
Best-fit parameters for the HYBRID model

Opacity (κ) (cm^2 g^{-1})	R_p[a] (10^{13} cm)	$M_{\rm ej}$[b] ($M_\odot$)	$M_{\rm csm}$[c] ($M_\odot$)	$\dot{M}$[d] ($M_\odot$ yr^{-1})	$M_{\rm Ni}$[b] ($M_\odot$)	$v_{\rm exp}$[b] (10^3 km s^{-1})	χ^2/DOF
0.10	30.42 ± 1.57	19.51 ± 0.22	29.56 ± 1.23	0.01 ± 0.001	2.05 ± 0.50	25.01 ± 0.06	0.76

Notes.
[a] R_p: progenitor radius before the explosion (in 10^{13} cm).
[b] discussed above.
[c] $M_{\rm csm}$: CSM mass (in $M_\odot$).
[d] $\dot{M}$: progenitor mass-loss rate (in $M_\odot$ yr^{-1}).

Table 4
Best-fit parameters for the HYBRIDW model

Opacity (κ) (cm^2 g^{-1})	R_p[a] (10^{13} cm)	$M_{\rm ej}$[a] ($M_\odot$)	$M_{\rm csm}$[a] ($M_\odot$)	$\dot{M}$[a] ($M_\odot$ yr^{-1})	$M_{\rm Ni}$[a] ($M_\odot$)	$v_{\rm exp}$[a] (10^3 km s^{-1})	χ^2/DOF
0.10	87.99 ± 7.91	15.33 ± 2.48	22.99 ± 0.99	0.64 ± 0.04	0.32 ± 0.26	24.99 ± 0.27	0.56

Note.
[a] Discussed above.

Imaging Spectrometer (LRIS; Oke et al. 1995) on the Keck-10m. A summary of the spectroscopic observations is given in Table 7, with a coverage of −28 to +194 days. The HET-9.2 m spectra were observed near the parallactic angle to minimize the effects of atmospheric dispersion. The Keck-10m spectra were obtained with an atmospheric dispersion corrector on LRIS, providing accurate relative spectrophotometry.

Data reduction was conducted with standard routines in IRAF,[18] including bias and flat-field corrections, wavelength calibration, and flux calibration. At the HET-9.2 m, HgCd and ArNe spectral lamps are used for wavelength determination, while a spectrum of a suitable spectrophotometric standard star was taken on every night for performing the relative-flux calibration. The Keck-10m spectra were reduced in a similar manner. In this section, the symbol Å is used for observed wavelengths and λ for rest-frame wavelengths.

It is clear from Figures 6 and 8 that the spectra of SN 2010kd could be considered in two parts. The first part consists of photospheric-phase spectra from −28 to +34 days; within this, four spectra belong to the hot photospheric phase (−28, −24, −23, and −22 days) and two spectra belong to the cool photospheric phase (+15 and +34 days). All spectra in the photospheric phase were observed using the HET-9.2 m. The second part covers three nebular-phase spectra observed at +96, +144, and +194 days. The spectrum at +144 days was observed using the HET-9.2 m and the other two (+96 and +194 days) were observed with the Keck-10m.

4.1. Photospheric-phase Spectra and `SYNAPPS` Spectral Matching

The photospheric-phase spectral evolution of SN 2010kd is plotted in Figure 6. Throughout the photospheric phase, the spectra of SN 2010kd are dominated by the hot blue continuum, having a BB temperature range of ∼20,000–10,000 K.

To explore possible identifications of the strong absorption lines, we modeled the first six spectra (−28, −24, −23, −22, +15, and +34 days) of SN 2010kd using the `SYNAPPS` code (Thomas et al. 2011), which is a revised and improved version of SYNOW (Jeffery & Branch 1990). We have modeled spectra in the photospheric phase, because at this phase, the spectra have the most prominent features; moreover, `SYNAPPS` only works in the photospheric phase, not in the nebular phase.

In Figure 6, we plot the observed spectra (in black) with the code-generated output synthetic spectra (in red). The ordinate plots λ^2 × flux density (F_λ) to highlight the spectral matching at longer wavelengths. In photospheric-phase spectra at shorter

---

[18] http://iraf.noao.edu/

Table 5
Best-fit Parameters for the CSMI-only Model

Opacity (κ) ($cm^2 g^{-1}$)	R_p [a] (10^{13} cm)	M_{ej} [a] ($M_\odot$)	M_{csm} [a] ($M_\odot$)	$\dot{M}$ [a] ($M_\odot yr^{-1}$)	M_{Ni} [a] ($M_\odot$)	v_{exp} [a] (10^3 km s^{-1})	χ^2/DOF
0.10	79.89 ± 4.54	18.47 ± 0.65	22.68 ± 0.53	0.62 ± 0.02	0.0 ± 0.0	24.75 ± 0.11	0.55

Note.
[a] Discussed above.

wavelengths, many lines overlap, so their observed widths do not adequately represent the ejecta velocity. At longer wavelengths, on the other hand, line densities are less severe, and individual lines can be identified clearly.

Photospheric-phase spectra of SN 2010kd mainly exhibit C II, C IV, O I, O II, Na I D, Mg II, Si II, and Fe II lines that are well reproduced by the code. No broad H or He lines are detected at any stage. Spectra in the hot photospheric phase exhibit a strong C II λ6578.05 line at ∼6350 Å, which weakens in the cool photospheric phase. In the hot photospheric phase, the C IV λ5801.31 line is also observed at ∼5530 Å, with a consistent blueshifted absorption trough at a velocity around 14,000 km s^{-1}; this line disappears in the cool photospheric phase.

It has been noticed that a large number of dense O II lines is one of the strongest features in the visible-light spectra of SLSNe I (Quimby et al. 2011, 2018). The W-shaped O II absorption lines are observed at ∼3980, 4200, and 4500 Å, at a velocity of around 12,000 km s^{-1}; they are the dominant features of most SLSNe I (Quimby et al. 2011). The O II λ4357.97 line observed at ∼4200 Å seems to have contributions from C II and Fe III in the hot photospheric-phase spectra. As temperature falls below ∼15,000 K, the spectra fall into the cool photospheric phase; O II features weaken and are overtaken by heavier elements such as Mg II and Fe II (Mazzali et al. 2016; Bose et al. 2018).

Spectra at the redder end typically show a much weaker feature of O I λ7774 at ∼7500 Å, but it may have some contribution from Mg II λ7877. Na I D absorption is not present in the spectra during the hot photospheric phase but appear substantially in the cool photospheric phase. The Si II λ6355 line is strong in the spectrum at −28 days with a velocity around 21,000 km s^{-1}. Spectra at +15 and +34 days have low- and high-velocity components of Si II and O II, possibly indicating nuclear burning fronts in the outer layers of the explosion (Hatano et al. 1999). Lines detected at lower velocity (∼11,500 km s^{-1}) represent freshly synthesized material whereas higher velocity (∼19,000 km s^{-1}) components are likely to be primordial, as suggested by Hatano et al. (1999).

In the hot photospheric-phase spectra, initially the Fe II λ5169 lines are blended and dominated by the hot blue continuum, but as the spectrum evolves from the hot to the cool photospheric phase, the Fe II lines strengthen and are observed at ∼4500–5200 Å. The contributions of individual ions to generate the spectra at −28 and +34 days are shown in Figure 7.

4.2. Evolution of Nebular-phase Spectra

As SNe continue to expand and cool, their ejecta eventually become transparent, and they enter the nebular phase. The nebular phase begins much later in SLSNe I ($\gtrsim$+90 days) compared to normal SNe Ic, indicating that high densities are sustained for a longer time period in the massive ejecta of SLSNe I (Nicholl et al. 2015a). The nebular spectra of SN 2010kd were taken at +96, +144, and +194 days (see Figure 8); line identification is based on that done by Inserra et al. (2017) and Jerkstrand et al. (2017).

Ions and spectral features seen in the nebular-phase spectra of SN 2010kd are indicated with arrows of different colors at their respective rest-frame wavelengths. Dominant O II and C II absorption lines in the photospheric-phase spectra are now weakened or have disappeared in the nebular phase; spectra are now dominated by O I and Ca II emission lines.

The region ∼5000–5800 Å shows a broad and blended emission feature of [O I] λ5577 and [Fe II]. The region ∼5800–6500 Å shows a trio of emission lines, possibly contributed by Na I D, Si II, and the [O I] $\lambda\lambda$6300, 6364 doublet. The O I λ7774 line has been observed at a velocity around 7000 km s^{-1}; it is a recombination line that decays from the lower state of an O I λ9263 transition. The nebular spectra of SN 2010kd exhibit a broad component of [O III] lines which Section 7.1 discusses in detail.

For SN 2010kd, the Mg I] line begins to appear feebly after ∼+34 days and strongly in the later nebular phases. The nebular-phase spectra of SN 2010kd show evolving Ca II H&K, [Ca II] $\lambda\lambda$7291, 7323, and Ca II $\lambda\lambda$8498, 8542, 8662 NIR triplet. The strength of the Ca II, O I, and Na I D absorption increases substantially in the nebular-phase spectra of SN 2010kd.

4.3. Evolution of Spectral Lines of SN 2010kd

Evolution of spectral features of SLSNe I provides important clues to the interaction of CSM with the expanding ejecta and other important properties like geometrical distribution and dust formation in the ejecta. To highlight the evolution of individual lines, a section of spectra is plotted in the velocity domain corresponding to the rest-frame wavelength of various elements (see Figure 9). The evolution of C II λ6578, C IV λ5801, O I λ7774, and O II $\lambda\lambda$4115.17, 4357.97, 4650.71 is presented. As the spectrum evolves, the minima of the absorption lines gradually move to lower velocities (i.e., toward redder wavelengths).

C II and C IV lines are present only in the hot photospheric-phase spectra; C II seems prominent relative to C IV and is well fitted with a single Gaussian. The C II and C IV line velocities estimated using the SYNAPPS spectral matching (see Figure 13) and Gaussian fitting are in good agreement, indicating that these lines are free from blending, not seen in the case of many other lines.

As spectra evolve from the photospheric to the nebular phase, the O I λ7774 line evolves in FWHM intensity, depth, and width; it also becomes stronger and sharper, similar to those seen in the case of SN Ic (Pastorello et al. 2010). The O I λ7774 line is well fitted with a single Gaussian, but the

Table 6
List of Well-studied SLSNe I at Comparable Redshift Used for the Photometric Comparison with SN 2010kd

	SLSN I	R.A. (α) (^{h}:^{m}:^{s})	Decl. (δ) (°:′: ″)	Redshift (z)	$E(B-V)$ (mag;Galactic)	$E(B-V)$[a] (mag;Host)	MJD$_{B,\mathrm{peak}}$	$M_{B,\mathrm{peak}}$ (mag)	Source
1	SN 2007bi	13:19:20.19	+ 08:55:44.3	0.128	0.02	0.04	54,159.47	-21.41 ± 0.09[b]	Gal-Yam et al. (2009), Young et al. (2010)
2	PTF10hgi/ SN 2010md	16:37:47.00	+ 06:12:32.3	0.098	0.07	0.01	55,367.43	-20.66 ± 0.04	Inserra et al. (2013), De Cia et al. (2018)
3	SN 2011ke/ PTF11dij/ PS1-11xk	13:50:57.77	+ 26:16:42.8	0.143	0.01	0.00	55,684.77	-21.04 ± 0.15	Inserra et al. (2013)
4	SSS120810: 231802 −560926	23:18:01.80	− 56:09:25.60	0.156	0.05	0.00	56,158.30	-21.29 ± 0.06	Nicholl et al. (2014)
5	PTF12dam	14:24:46.20	+ 46:13:48.3	0.107	0.01	0.02	56,093.70	-21.68 ± 0.07	Nicholl et al. (2013), Chen et al. (2015)
6	SN 2015bn	11:33:41.57	+ 00:43:32.2	0.114	0.02	0.30	57,103.38	-23.21 ± 0.10	Nicholl et al. (2016b)
7	Gaia16apd/SN 2016eay	12:02:51.71	+ 44:15:27.4	0.101	0.01	0.01	57,549.59	-21.86 ± 0.05	Kangas et al. (2017), Nicholl et al. (2017)

Notes.

[a] For all the tabulated SLSNe I, the host-galaxy extinction values are taken from Schulze et al. (2018) except for Gaia16apd (Kangas et al. 2017).

[b] $M_{R,\mathrm{peak}}$ is taken in place of $M_{B,\mathrm{peak}}$.

estimated parameters are not reliable because of possible Mg II λ7877 blending. The O II lines seem to shift redward with phase, showing decreasing velocity; however, velocity estimates using single-Gaussian fitting are not reliable when considering blended features. It is best to use `SYNAPPS` spectral matching for blended features.

4.4. Temperature and Radius Evolution of SN 2010kd

In this section, we discuss the evolution of the BB temperature (in red) and radius (in blue) of SN 2010kd derived from the photometric and spectroscopic data (see Figure 10). We calculate the photospheric temperature and radius evolution by modeling the SED at possible epochs by fitting a BB function using the code `Superbol` (Nicholl 2018). The temperature and radius values estimated using the BB fit individually to the spectra are also shown. Overall, the temperature and radius evolution calculated from two different methods are in good agreement.

At premaximum phases (from ~-28 to -15 days), the temperature of SN 2010kd decays sharply from ~20,000 to 17,000 K, whereas around the time of peak brightness (from ~-15 to $+15$ days) the temperature seems nearly constant. After peak brightness, from $\sim+15$ to $+80$ days, the temperature decays from ~15,000 to 8000 K, and at later phases (after $\sim+80$ days), it decays shallower (~5 K per day) relative to the decay rate at early phases.

From ~-28 to $+50$ days, the radius of SN 2010kd sharply increases (from $\sim(1.8 \text{ to } 4.0) \times 10^{15}$ cm), whereas it decreases slowly ($\sim 0.03 \times 10^{15}$ cm per day) after $\sim+80$ days. The photospheric temperature of SN 2010kd during the earliest phases ($>$12,000 K) seems to be somewhat hotter than that of PTF12dam and SN 2015bn ($\lesssim$12,000 K; Nicholl et al. 2016b). The BB radius estimated for SN 2010kd is smaller in comparison to SN 2015bn (from $\sim(8 \text{ to } 12) \times 10^{15}$ cm) and decays comparatively shallower after +50 days (Nicholl et al. 2016b).

5. Spectral Comparison of SN 2010kd with Other H-deficient SNe

SLSNe I spectra near peak brightness exhibit differences in several features among the two populations i.e., slow and fast decaying (Nicholl et al. 2016b; Quimby et al. 2018). Hence, in the next two sections, we compare the spectra of SN 2010kd with the template spectra of slow- and fast-decaying SLSNe I. To study the spectral diversity among SNe Ic and SLSNe I, we compared the spectra of SN 2010kd with a subset of well-studied broad-lined SNe Ic.

5.1. Comparison of SN 2010kd with Slow-decaying SLSNe I

In this section, observed spectra of SN 2010kd are compared with three slow-decaying SLSNe I: SN 2007bi (Gal-Yam et al. 2009, in green), PTF12dam (Nicholl et al. 2013, in blue), and SN 2015bn (Nicholl et al. 2016b, in red); see Figure 11. All of the plotted spectra have been shifted to their respective rest-frame wavelengths. For a significant comparison, spectra of PTF12dam and SN 2015bn are chosen at epochs close to those of the spectra of SN 2010kd. As shown in Figure 11, the spectral evolution of SN 2010kd appears to be an excellent match to those of SN 2007bi, PTF12dam, and SN 2015bn; however, there are also some petty differences.

In the two upper panels of Figure 11, the photospheric spectra of SN 2010kd at -28 and $+34$ days are compared with PTF12dam and SN 2015bn. All of the colored vertical lines are plotted at the observed wavelengths of various elements, associated with their respective colors. In the photospheric phase, the continuum temperature of SN 2010kd looks hotter than that of PTF12dam and SN 2015bn, as discussed in Section 4.4. The spectra of SN 2010kd and SN 2015bn are consistent for a longer time around maximum light than PTF12dam. This may be because of their shallower velocity decay rates in comparison to PTF12dam (see Figure 13).

Both SN 2010kd and PTF12dam have a C II line around the same velocity (Quimby et al. 2018), whereas SN 2015bn only has a meager signature of this line (Nicholl et al. 2016b). SN

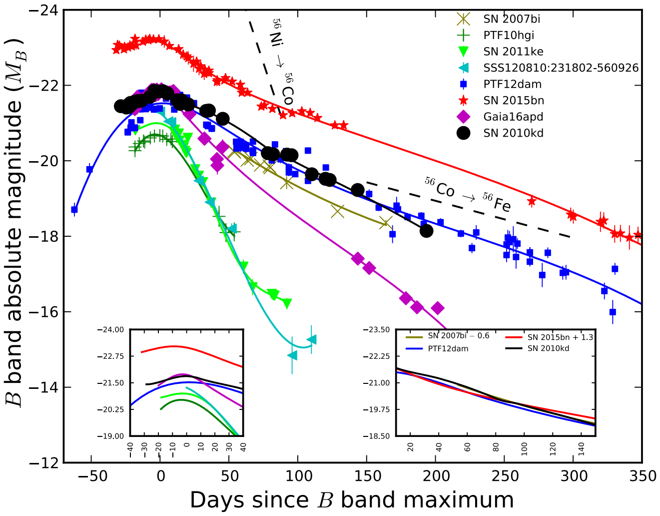

Figure 3. The B-band absolute magnitudes of SN 2010kd (in black) are compared with a subset of well-studied SLSNe I at comparable redshift, as listed in Table 6. We also compare these light curves with the ^{56}Ni → ^{56}Co and ^{56}Co → ^{56}Fe theoretical decay curves, shown with black dotted lines. The B-band light curve of SN 2010kd nearly traces the decay pattern shown by SN 2007bi, PTF12dam, and SN 2015bn, representing slow-decaying SLSNe I.

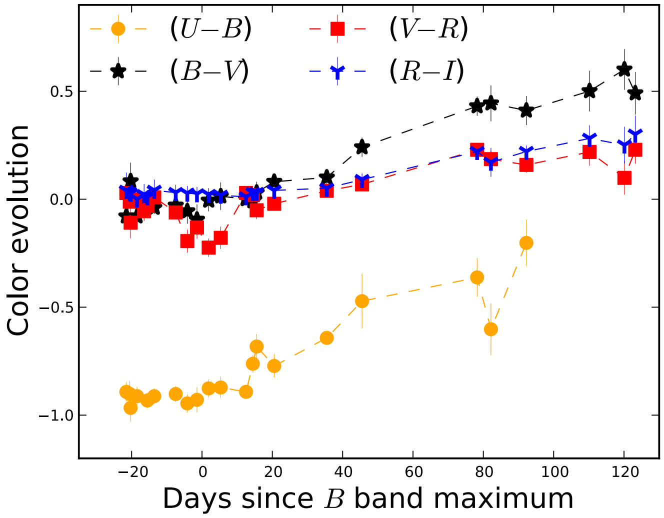

Figure 4. The $(U-B)$, $(B-V)$, $(V-R)$, and $(R-I)$ color curves of SN 2010kd are plotted. The $(B-V)$, $(V-R)$, and $(R-I)$ color curves show nearly similar behavior and turn redder very slowly with respect to the $(U-B)$ color curve. The negative value of the $(U-B)$ color shows that SN 2010kd is brighter in the U band in comparison to the B, V, R, and I bands.

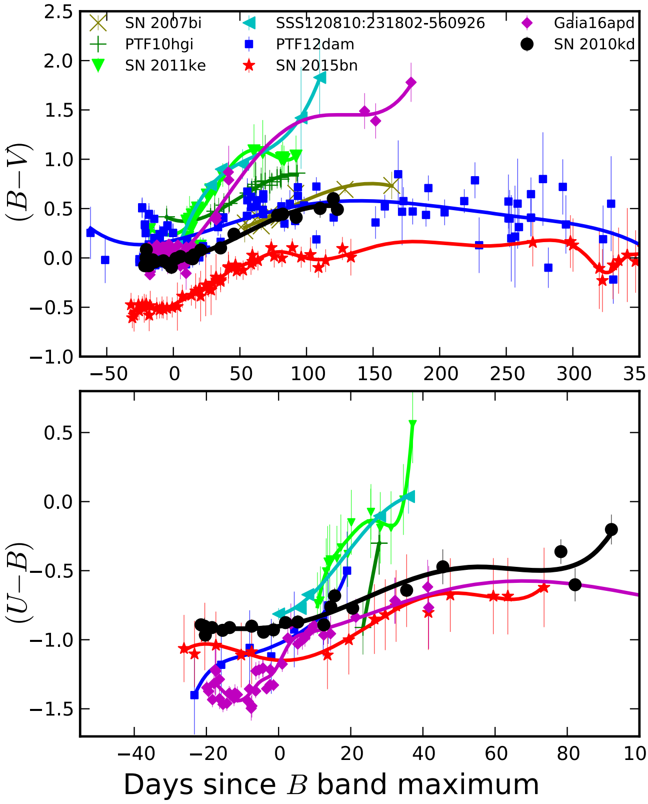

Figure 5. Upper panel: the $(B-V)$ color curve of SN 2010kd is compared with the SLSNe I listed in Table 6. The $(B-V)$ color evolution of SN 2010kd becomes redder slowly in comparison to the fast-decaying SLSNe I and appears to trace the path of slow decliners. Lower panel: the $(U-B)$ color evolution of SN 2010kd is compared with the slow-decaying SLSNe I, fast-decaying SLSNe I, and one intermediate SLSN, Gaia16apd.

2015bn shows C IV λ5801.31 weaker than SN 2010kd, but Nicholl et al. (2016b) claimed it as an unidentified line or a Si II line of very high velocity. In early-time spectra, PTF12dam also exhibits a weak trough of this line at ∼5750 Å, but Quimby et al. (2018) claimed this feature as an unidentified line, or He λ5876. SN 2010kd, PTF12dam, and SN 2015bn seem to have have similar O I λ7774 line evolution, whereas the lack of O I could be a distinguishing difference between the slow- and fast-decaying SLSNe I (Quimby et al. 2018). The hot photospheric-phase spectra of SN 2010kd and PTF12dam have stronger O II lines (Quimby et al. 2018), whereas in SN 2015bn these lines are comparatively weaker even at −25 days (Nicholl et al. 2016b). However, in the case of SN 2010kd and SN 2015bn, the O II λ4357.97 line is blended with Fe III λ4420, which is not significant in the case of PTF12dam (Nicholl et al. 2016b). The centers of absorption troughs show that the velocity of the O II lines in SN 2015bn appear to be lower compared to SN 2010kd and PTF12dam.

In the lower panel of Figure 11, three nebular spectra of SN 2010kd are compared with the nebular spectra of SN 2007bi, PTF12dam, and SN 2015bn. The nebular phase in SLSNe I starts after ∼+90 days, but we also included the +47 day spectrum of SN 2007bi because it seems to have many similar lines (except [O III] λ5007) as in the +96 day spectrum of SN 2010kd.

For SN 2010kd, the blending of [O I] with [Fe II] lines seems to increase with phase, as can also be seen in spectra of SN 2007bi, PTF12dam, and SN 2015bn. SN 2010kd and SN 2015bn have stronger [O III] λλ4959, 5007 broad emission lines in comparison to PTF12dam, whereas [O III] λ4363 is absent in the early-phase (at +47 days) spectrum of SN 2007bi.

In summary, high-cadence, early-time spectra exhibit a small degree of diversity among these objects, but spectroscopic evolution of SN 2010kd overall confirms the similarity of this object to SN 2007bi, PTF12dam, and SN 2015bn.

5.2. Comparison of SN 2010kd with Fast-decaying SLSNe I

In this section, we compare the same sequence of spectra of SN 2010kd with three well-studied fast-decaying SLSNe I: PTF10hgi (Inserra et al. 2013, in red), SN 2011ke (Inserra et al. 2013, in blue), and SSS120810:231802–560926 (Nicholl et al. 2014, in green). For a significant comparison in the nebular

Table 7
Log of the Spectroscopic Observations of SN 2010kd

Date (UT)	MJD	Phase[a] (days)	Instrument	Wavelength (Å)	Resolution (Å)	Exposure Time (s)	Airmass	Telescope
2010 Nov 22	55,522.510	−28	LRS	4200–9004	4.51	900	1.24	HET-9.2 m
2010 Nov 26	55,526.487	−24	LRS	4200–10,200	4.51	1200	1.28	HET-9.2 m
2010 Nov 27	55,527.476	−23	LRS	4200–10,200	4.51	900	1.32	HET-9.2 m
2010 Nov 28	55,528.513	−22	LRS	4200–10,200	4.51	900	1.17	HET-9.2 m
2011 Jan 4	55,565.392	+15	LRS	4200–10,200	4.51	1200	1.24	HET-9.2 m
2011 Jan 23	55,584.353	+34	LRS	4200–10,200	4.51	1200	1.20	HET-9.2 m
2011 Mar 26	55,646.284	+96	LRIS	3038–10,233	1.07	700	1.30	Keck-10m
2011 May 13	55,694.270	+144	LRS	4200–10,200	4.51	2200	1.24	HET-9.2 m
2011 Jul 2	55,744.266	+194	LRIS	3250–10,100	1.07	970	1.35	Keck-10m

Note.
[a] Phase is given in days since *B*-band maximum.

phase, we cover a range from +59 to +265 days. As can be seen from the upper panel of Figure 12, SN 2010kd maintained a strong blue continuum for a much longer time relative to the fast-decaying SLSNe I, which exhibit a redder continuum even at ∼+36 days.

The fast-decaying SLSNe I seem to have smoother spectra in comparison to SN 2010kd, indicating broader velocity distributions which blend and smooth out individual lines (Quimby et al. 2018). SN 2010kd appears to have sharper absorption lines and higher emission-line luminosities in the nebular phase with respect to the fast-declining SLSNe I.

Despite the above-mentioned differences, both classes of SLSNe I exhibit nearly the same lines and in the same order of strength, mainly calcium, Mg I], and [Fe II]. These lines become prominent at early phases (from ∼+36 days) in the fast-decaying SLSNe I, but at later phases (∼+96 days) in objects like SN 2010kd owing to their slower photometric evolution. Spectra of photometrically fast-decaying SLSNe I seem to evolve faster in comparison to SN 2010kd. The result is that the spectra of fast-decaying SLSNe I at ∼+100 days seem to differ from spectra of slow-decaying SLSN at ∼+100 days and are better matched to the slow decliners at ∼+200 days, as also suggested by Quimby et al. (2018). Slower spectral evolution of slow-declining SN 2010kd might indicate higher ejecta mass and more slowly decreasing velocities in comparison to the fast-declining SLSNe I.

5.3. Comparison of SN 2010kd with Broad-lined Type Ic SNe

In this section, we compare the nebular-phase spectra of SN 2010kd (in black) with spectra of two well-studied Type Ic-BL SNe: SN 1998bw (Sollerman et al. 2000, in green) and SN 2002ap (Vinko et al. 2004, in red); see the lower panel of Figure 12. SN 1998bw is a broad-lined event associated with a long/soft GRB (SN Ic-BL + LGRB), whereas SN 2002ap is a broad-lined SN Ic with no associated GRB (SN Ic-BL). SN 2002ap seems to evolve much faster than SN 1998bw and SN 2010kd. The spectrum of SN 2002ap at +32 days appears similar to the spectrum of SN 1998bw at +72 days and that of SN 2010kd at +194 days. The nebular-phase spectra of SN 2010kd seem to evolve slower in comparison to SN 1998bw and SN 2002ap, as studied in the case of other slow-decaying SLSNe I (Nicholl et al. 2016a; Jerkstrand et al. 2017).

SN 1998bw and SN 2002ap exhibit similar major spectral features to SN 2010kd (except in the region ∼5700–6500 Å), but different behavior in terms of the shape and density of the line features. At phases ∼+90 to +200 days, in the range ∼5700–6500 Å, the most important line for comparison is the [O I] doublet, generally the strongest feature in nebular spectra of SNe Ic and not severely contaminated by other lines. In this range, SN 2010kd shows the trio of Si II, Na I D, and the [O I] doublet (shaded with gray color), which can be seen in nebular-phase spectra of most SLSNe I (see Figure 11). As suggested by Nicholl et al. (2016b), we can take this trio as a real spectroscopic difference between spectra of SLSNe I and SNe Ic. SN 2010kd reveals weak [O I] λλ6300, 6364 in all three nebular spectra, but this line could become very prominent at late phases (after ∼300 days) as shown by Jerkstrand et al. (2017) for SN 2015bn. The broad [O III] λ4363 and λλ4959, 5007 emission lines are strong in SN 2010kd, whereas SN 1998bw and SN 2002ap do not have any evidence of these lines.

The other significant difference is in the calcium and magnesium spectral lines. SN 1998bw and SN 2002ap show strong emission lines of Mg I], Ca II H and K, [Ca II], and the Ca II NIR triplet compared to SN 2010kd (shaded with pink and gold colors). SN 2002ap has the strongest Mg I] line in comparison to SN 1998bw and SN 2010kd. Spectra of SN 2002ap and SN 1998bw show a clear blending of the [O II] λ7235 line with [Ca II] up to late phases, whereas this blend is not clear in SN 2010kd.

All three SNe have [Fe II] λ5250, but this line is again strongest in SN 2002ap. [Fe II] is blended with [O I] λ5577 in the spectra of SN 2010kd, which is not significant in plotted SNe Ic-BL. The O I λ7774 line is most prominent in SN 2010kd in comparison to SN 1998bw and SN 2002ap.

In summary, we can say that SN 2010kd evolves comparatively slower and seems to have many lines similar to those of SNe Ic-BL but with different intensities. This indicates a clear diversity in the nebular-phase spectra of SLSNe I and SNe Ic-BL, an important key to understanding the diverse underlying physical mechanisms in different types of SNe Ic.

6. Line-velocity Comparison of SN 2010kd with Other SLSNe I

In this section, we determined line velocities of SN 2010kd using `SYNAPPS` spectral matching and compared them with a set of well-studied SLSNe I at comparable redshift; see Figure 13. Line velocities of SN 2007bi (Young et al. 2010; Liu et al. 2017), PTF10hgi (Liu et al. 2017), SN 2011ke (Inserra et al. 2013; Liu et al. 2017), SSS120810:231802–560926 (Liu et al. 2017),

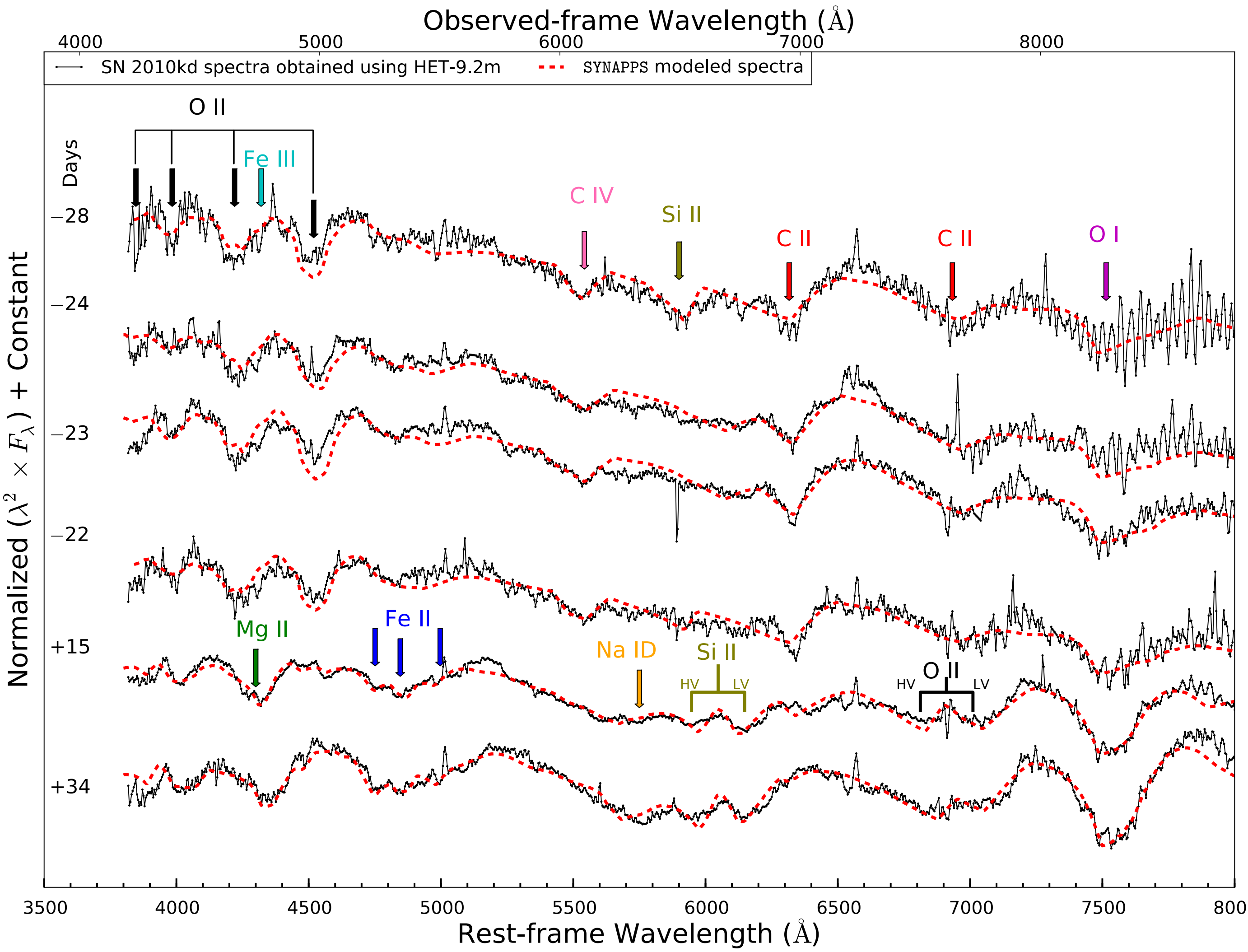

Figure 6. Photospheric-phase spectral evolution of SN 2010kd (in black) along with the SYNAPPS (Thomas et al. 2011) spectral matching (in red) is plotted. Data have been corrected for the Galactic extinction and redshift. All spectral features are marked by vertical arrows at the observed-frame wavelengths of the elements, as given in their respective colors. The blue parts of the spectra are dense with O II absorption lines. All six photospheric-phase spectra of SN 2010kd are well reproduced with the SYNAPPS code.

PTF12dam (Nicholl et al. 2016b; Quimby et al. 2018), and SN 2015bn (Nicholl et al. 2016b) are plotted for comparison.

For SN 2010kd, the velocity evolution of the C II, C IV, O I, O II, Na I D, Mg II, and Fe II lines are plotted. In the photospheric phase (from −28 to +34 days), all lines show nearly constant velocity curves having a range of ∼12,500–11,000 km s^{-1}, except C IV, which has the highest velocity around 14,000 km s^{-1}. In the photospheric phase, the velocity of the O I λ7774 line remains almost constant, which is commonly observed in other SLSNe I as well (Nicholl et al. 2015a, 2016b); see Figure 13. The O I line velocities at nebular phases are calculated using single-Gaussian fitting, because we cannot use SYNAPPS at such late phases. The constant velocity evolution possibly indicates stratification of line-forming shells within a homologous expansion. The C II, C IV, Na I D, Mg II, and Fe II lines also show a shallow decline in velocity with time (∼200 km s^{-1} every 10 days). In the case of SN 2010kd, the relation between the estimated velocity of the Fe II λ5169 line at ∼+10 days ($\lesssim$12,000 km s^{-1}) and its decay rate between ∼+10 and ∼+30 days (∼30 km s^{-1} day^{-1}) is in good agreement with those observed in the case of other slow-decaying SLSNe I (Inserra et al. 2018b).

The O II line velocity of SN 2010kd is nearly constant (∼12,000 km s^{-1}) in comparison to PTF12dam, which has a declining O II line velocity (from ∼11,000 to 7000 km s^{-1}) with a rate of ∼1200 km s^{-1} per 10 days. The O I line velocity of SN 2010kd nearly traces the path estimated for PTF12dam.

The evolution of the Fe II line velocity of SN 2010kd is almost flatter in comparison to the fast-decaying SLSNe I (PTF10hgi, SN 2011ke, and SSS120810:231802–560926), which indicates that photometrically fast-decaying SLSNe I have comparatively faster-declining Fe II line velocities (Inserra et al. 2018b).

In summary, SN 2010kd has flatter velocity curves in comparison to SN 2007bi, PTF12dam, and other fast-decaying SLSNe I, but similar velocity evolution to that seen in the case of SN 2015bn. The flat velocity curves of SN 2010kd might indicate possible signature of a central engine accelerating the inner ejecta as suggested by Nicholl et al. (2016b) for SN 2015bn.

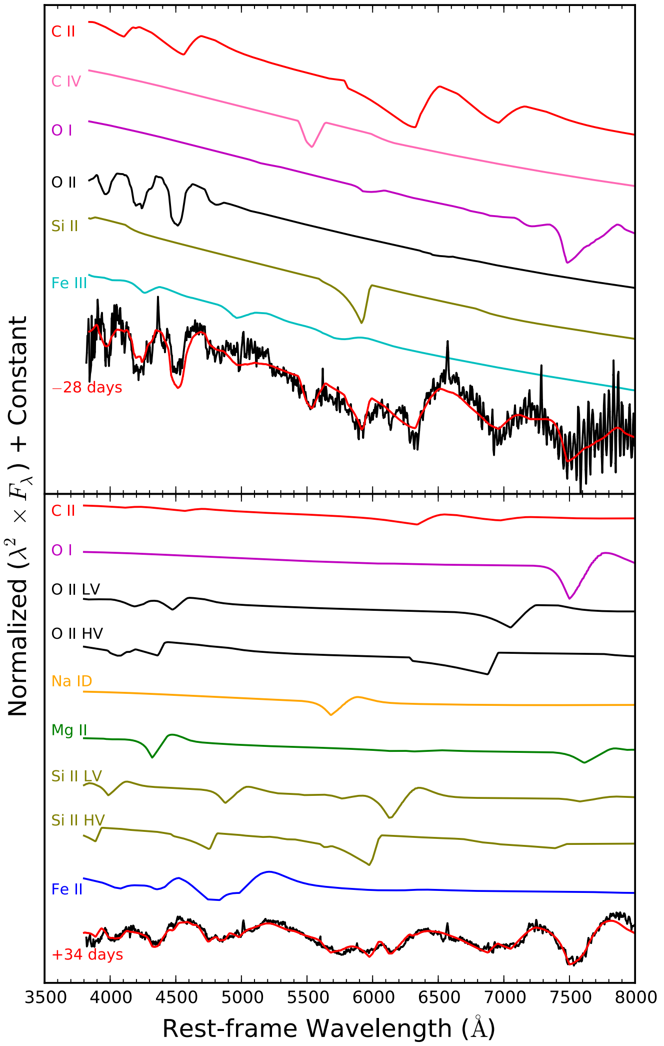

Figure 7. Single-ion contributions to match the spectra of SN 2010kd at −28 and +34 days using the `SYNAPPS` code are presented. In the spectrum at +34 days, the low- and high-velocity components of the O II and Si II lines are also found.

7. Line Luminosities in the Nebular Phase

In this section, we present integrated luminosities of various emission lines in nebular spectra of SN 2010kd: [O I] $\lambda5577$, [O I] $\lambda\lambda6300, 6364$, O I $\lambda7774$, Mg I] $\lambda4571$, [Ca II] $\lambda\lambda7291$, 7323, and the Ca II NIR triplet (see Figure 14, in black). First, the continuum was subtracted by a linear fit, and the values of luminosities are estimated by direct numerical integration only for the lines that are isolated and do not have highly blended features, except [O I] $\lambda5577$. For the [O I] $\lambda5577$ line, we fitted a double Gaussian, because it is blended with [Fe II] $\lambda5250$, the same method adopted by Nicholl et al. (2019). We also attempted subtracting the contribution of the host-galaxy flux from the nebular-phase spectra of SN 2010kd using the host spectrum published by Leloudas et al. (2015) as described by Nicholl et al. (2019); however, the host-galaxy continuum flux of SN 2010kd is found to be negligible.

In the case of SN 2010kd, the luminosity of the strongest lines is $\sim10^{42}$ erg s^{-1} at +96 days, dropping to $\sim4 \times 10^{40}$ erg s^{-1} at +194 days, consistent with the result of Nicholl et al. (2019) for different SLSNe I. For SN 2010kd at early epochs, Mg I] has the highest luminosity, followed by [Ca II], the Ca II NIR triplet, and O I $\lambda7774$; the rest of the lines have even lower luminosities.

We compare luminosities of various lines of SN 2010kd with a set of well-studied SLSNe I (see Figure 14). All of the published comparison data were taken from Nicholl et al. (2019 and references therein; Nicholl et al. 2013, 2016a, 2016b, 2017; Chen et al. 2015; Inserra et al. 2017; Jerkstrand et al. 2017; Kangas et al. 2017; Quimby et al. 2018). In the present study, for comparison we mainly discuss the line-luminosity evolution of PTF12dam and SN 2015bn, because these SLSNe I have a significant number of spectroscopic data points and are also at comparable redshifts. Line-luminosity values of these objects are fitted with straight lines.

Throughout this section, the line luminosity is in units of 10^{41} erg s^{-1}, whereas the decay rate is in 10^{41} erg s^{-1} every 100 days. Line luminosities are compared at early phases (∼+96 days), because at later phases, the luminosity values seem to converge. The [O I] $\lambda\lambda6300, 6364$ line luminosity is lower for SN 2010kd (∼3.85) in comparison to PTF12dam (∼7.20) and SN 2015bn (∼5.75), whereas the decay rate is nearly the same for SN 2010kd and PTF12dam (∼2.80). The O I $\lambda7774$ line luminosity of PTF12dam is higher (∼1.10), with a steeper decay rate (∼5.15) relative to SN 2010kd and SN 2015bn. SN 2010kd shows higher line luminosities of the [Ca II] and Mg I] lines, and steeper decay rates in comparison with other SLSNe I. In the case of [O I] $\lambda5577$, PTF12dam and SN 2015bn have almost constant decay rates (∼0.70) in comparison to the decay rate (∼1.90) for SN 2010kd.

In Figure 15, luminosity ratios of key diagnostic lines are plotted. [O I] $\lambda5577$, O I $\lambda7774$, Mg I], [Ca II], and the Ca II NIR triplet are normalized to the luminosity of the [O I] $\lambda\lambda6300, 6364$ doublet. The [Ca II] line luminosity is normalized also with the Ca II NIR triplet luminosity. Line-luminosity ratios show that the luminosities of all presented lines are ∼1–3 times the [O I] $\lambda\lambda6300, 6364$ luminosity, except for [O I] $\lambda5577$/[O I] $\lambda\lambda6300, 6364$. Luminosity ratios at early phases (at +96 days) appear to have a larger range of values but converge at later epochs (+194 days). Like other slow-decaying SLSNe I, the [O I] doublet in SN 2010kd appears to have less luminosity in comparison to [Ca II] $\lambda7300$ and evolve much later, which indicate a central engine power source heating the inner ejecta as suggested by Nicholl et al. (2019).

We also compared the line-luminosity ratios of various lines of SN 2010kd with other SLSNe I. SN 2010kd has approximately the same range of values as other SLSNe I for $L_{7774}/L_{6300,\,6364}$, $L_{7300}/L_{6300,\,6364}$, $L_{\mathrm{Ca\,II\,NIR}}/L_{6300,\,6364}$, and $L_{7300}/L_{\mathrm{Ca\,II\,NIR}}$. In comparison to PTF12dam and SN 2015bn, SN 2010kd has a high $L_{5577}/L_{6300,\,6364}$ luminosity ratio with a nearly similar decay rate, and high $L_{4571}/L_{6300,\,6364}$ with sharper decay rate.

We calculated some physical parameters of SN 2010kd using these luminosity ratios, as done by Jerkstrand et al. (2014) and Nicholl et al. (2019) for other SLSNe I. For SN 2010kd, $L_{5577}/L_{6300,\,6364}$ is ∼0.5–1.0, which is higher than those of other SLSNe I: ∼0.1–0.2 (see Figure 15). We assume that [O I] $\lambda5577$ and the [O I] doublet are from the same zone, so their ratio will depend only on optical depth and temperature. Thus, the ratio of these lines can indicate the single-zone local thermodynamic equilibrium (LTE)

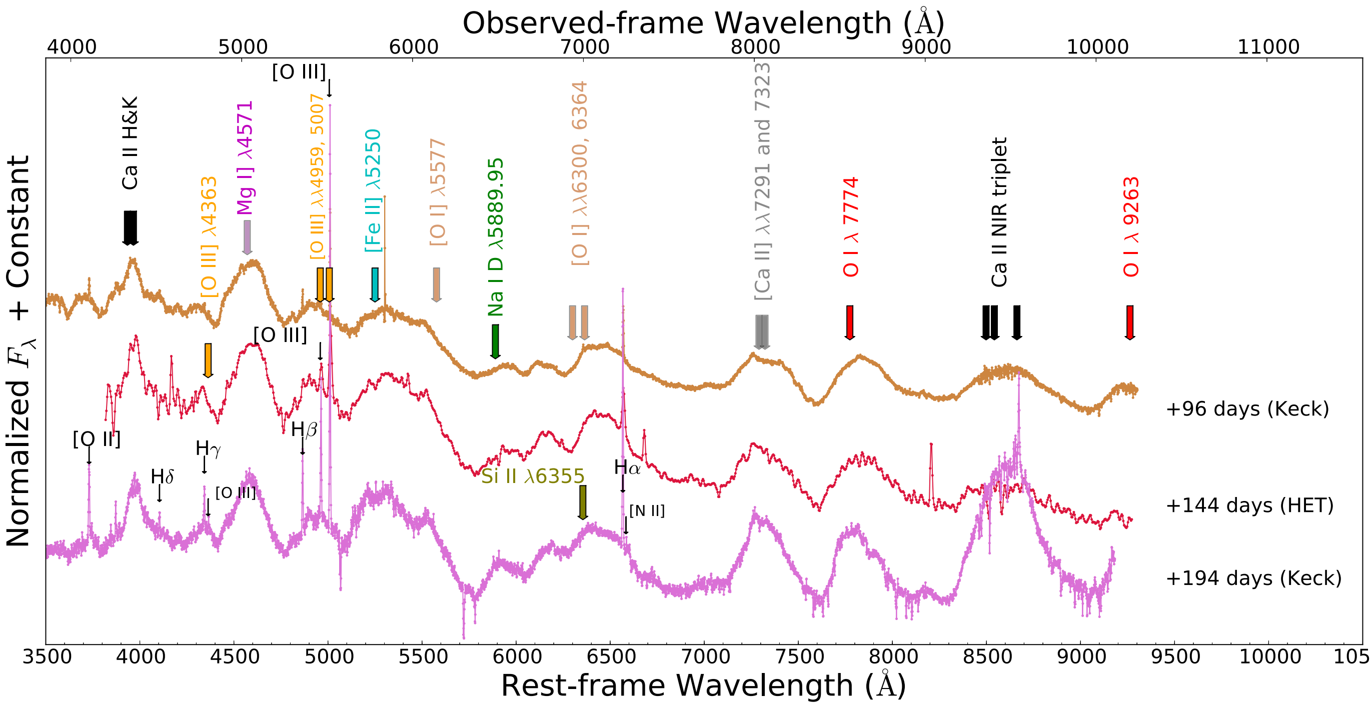

Figure 8. Rest-frame spectral evolution of SN 2010kd in the nebular phase (+96, +144, and +194 days) is plotted. Data have been dereddened and shifted to the rest-frame wavelengths. All spectral features are marked by vertical arrows at their rest-frame wavelengths, as represented by respective colors. In the spectrum at +194 days, the host-galaxy emission lines are marked with narrow black arrows. Nebular-phase spectra of SN 2010kd are dominated by O I and Ca II lines.

temperature, as discussed by Jerkstrand et al. (2017), Nicholl et al. (2019). To calculate the temperature, we used Equation (2) from Jerkstrand et al. (2014) and assume $\beta_{\rm ratio} = 1.5$. The temperature estimated for various SLSNe I using nebular-phase spectra after +200 days is $\lesssim$5000 K (Jerkstrand et al. 2014; Nicholl et al. 2019). But SN 2010kd has a very high single-zone LTE temperature (~6000 K), estimated using spectra at +96, +144, and +194 days (see Table 8). In summary, SN 2010kd has a higher $L_{5577}/L_{6300,\,6364}$ luminosity ratio as well as a high single-zone LTE temperature in comparison to the other SLSNe I presented in this study.

In stripped-envelope SNe, the oxygen ejecta mass is ~70% of the total $M_{\rm ej}$ (Maurer & Mazzali 2010). We can estimate the O I ejected mass using the luminosity ratio L_{6300}/L_{6364} (Jerkstrand et al. 2014). Unfortunately, our SN 2010kd spectra have low signal-to-noise ratio, so we are unable to measure L_{6300}/L_{6364}. However, we can estimate the upper limit of the O I ejected mass by comparing the luminosity of the [O I] λλ6300, 6364 blend. Jerkstrand et al. (2017) explained that the spectra of SN 2007bi, LSQ 14an, and SN 2015bn can be reproduced only by a model having oxygen mass $\gtrsim 10\,M_\odot$. Nicholl et al. (2019) compared the [O I] λλ6300, 6364 line luminosity of many SLSNe I (plotted in Figure 15) including SN 2007bi, LSQ 14an, and SN 2015bn and gave an upper limit of O I ejected mass $\sim 10\,M_\odot$. Similarly, we compared the [O I] λλ6300, 6364 line luminosity of SN 2010kd with a set of well-studied SLSNe I; see the upper-left panel of Figure 14. We can see clearly that the [O I] λλ6300, 6364 line luminosity of SN 2010kd is lower than that of SN 2007bi, PTF12dam, LSQ 14an, and SN 2015bn, and higher than that of SN 2017egm. So, for SN 2010kd, the upper limit of O I ejected mass is $\sim 10\,M_\odot$. This result is in good agreement with the total $M_{\rm ej}$ value calculated using the `Minim` fitting to the light curve of SN 2010kd (see Section 2.3).

7.1. Study of [O III] Lines in the Nebular Phase of SN 2010kd

The nebular spectra of SN 2010kd show broad emission features around 4360–5000 Å; we identify them as broad components of the [O III] λ4363 and [O III] λλ4959, 5007 lines (see Figure 16) as noticed in the case of PS1-14bj by Lunnan et al. (2016). We did not calculate their velocity because of blending with host-galaxy emission lines. We measured the flux ratio $f_{4959,\,5007}/f_{4363}$ for three nebular spectra of SN 2010kd, which could provide information about the electron density of the emitting region (Osterbrock & Ferland 2006).

Fluxes were calculated using a single-Gaussian fit to [O III] λ4363 and a double Gaussian fit to [O III] λλ4959, 5007. We estimated the values of $f_{4959,\,5007}/f_{4363} \approx 1.6$, 3.8, and 3.7 using the nebular-phase spectra at +96, +144, and +194 days, respectively. For PS1-14bj, Lunnan et al. (2016) reported this ratio to be $\lesssim 3$ and claimed that the electron density in the [O III]-emitting region is close to the critical density for these transitions ($>10^6$ cm^{-3}). For slow-evolving LSQ 14an, Inserra et al. (2017) claimed $f_{4959,5007}/f_{4363} \approx 1.8$, nearly equal to the value for SN 2010kd at +96 days. Using the spectrum of SN 2010kd at +96 days, we found a temperature $T \approx 8000$ K, corresponding to an electron density of $\sim 6.0 \times 10^7$ cm^{-3} for the medium. This electron density is estimated using the formula from Osterbrock & Ferland (2006) or Equation (1) of Inserra et al. (2017).

As shown in Figure 16, the peak of the [O III] λ4363 line is blueshifted relative to the rest-frame wavelength. Similarly, the [O III] λλ4959, 5007 lines have centroids that appear blueshifted in comparison to the rest-frame wavelength, showing velocities of ~3000 km s^{-1}.

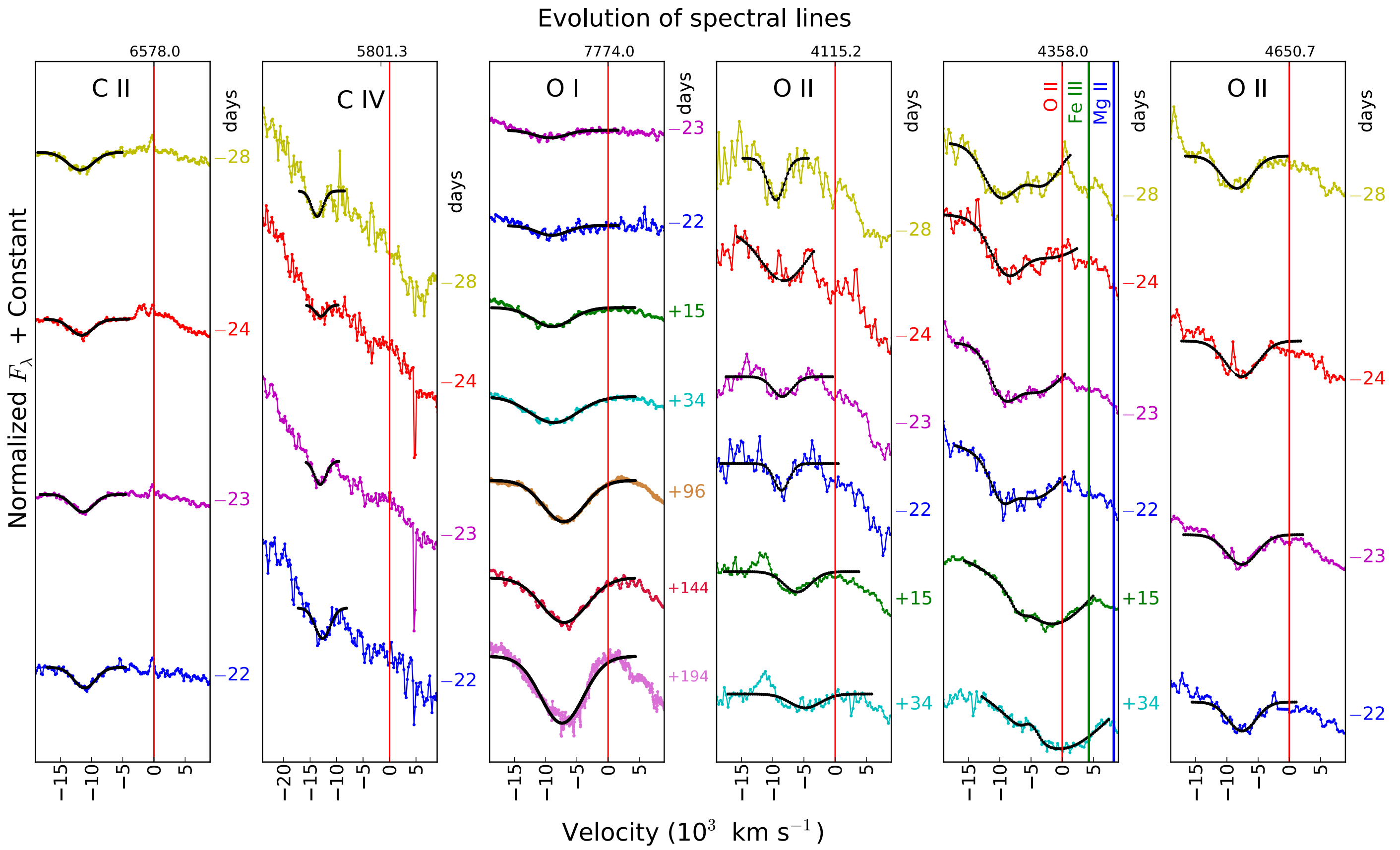

Figure 9. Evolution of the C II, C IV, O I, and O II lines is plotted. Zero velocity is marked with a vertical line (in red), and the corresponding rest-frame wavelength is written on top. The phases of plotted spectra are −28, −24, −23, −22, +15, +34, +96, +144, and +194 days (from top to bottom). For every particular feature, the section of spectra is shown only for those phases in which it is visible. All lines are fitted with a single-Gaussian function (in black) except O II λ4357.97, which seems to be blended with Mg II and Fe III lines and is fitted with a double Gaussian. All lines seem to have decreasing velocity as the phase increases.

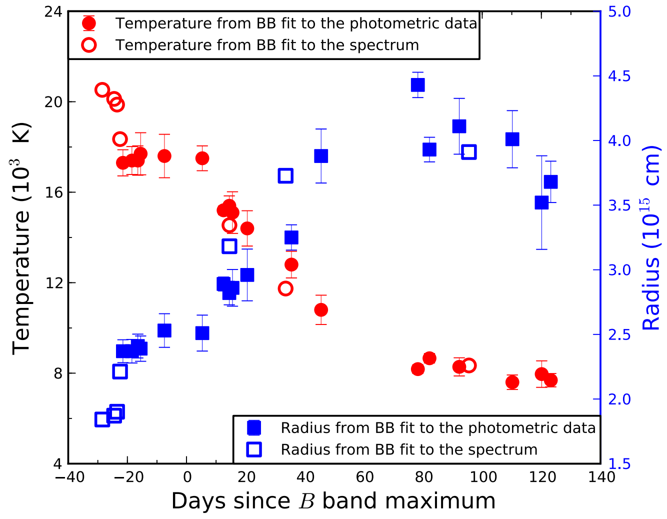

Figure 10. Evolution of the BB temperature and radius of SN 2010kd as derived from the photometric data using `Superbol` is plotted along with the temperature and the radius evolution calculated using the direct BB fit to the spectra. The temperature falls from ∼20,000 to 8000 K from the hot photospheric to the nebular phase, whereas the photospheric radius continuously increases from −28 to ∼+50 days and decreases slowly at later epochs.

8. Host Galaxy of SN 2010kd

Photometric and spectral studies of SLSN host galaxies provide enormous information about the nature of the environment and possible progenitors. On the basis of host-galaxy studies, Neill et al. (2011) were the first to discuss that SLSNe tend to occur in low-mass galaxies with high specific star formation rates (specific SFRs). Thereafter, Chen et al. (2013) found the host of SN 2010gx to be one of the lowest metallicity dwarf galaxies. On the basis of a systematic sample study of 30 SLSN hosts, Lunnan et al. (2014) showed that the host galaxies of SLSNe I are dwarfs similar to GRB hosts, with low luminosities. Later, many authors studied samples of known hosts of SLSNe I and found that they have lower metallicities and higher SFRs (Leloudas et al. 2015; Angus 2017; Perley et al. 2016; Chen et al. 2017b; Schulze et al. 2018).

In the present study, the host galaxy of SN 2010kd observed by *Swift*-UVOT in the *u* band at an apparent magnitude of 21.54 ± 0.23 (with a 4.7σ significance level; see Table 11 in Appendix A.1) is used to constrain the SFR. As discussed by Lunnan et al. (2014) and Angus (2017), the SFR of the host of SN 2010kd can be constrained using the rest-frame UV flux with the formula

$$\mathrm{SFR} = 1.4 \times 10^{-28} \times L_u(\mathrm{erg\ s^{-1}\ Hz^{-1}}) \quad (2)$$

(Kennicutt 1998). The derived value of the SFR of the host of SN 2010kd is ∼$0.18 \pm 0.04\,M_\odot$ yr^{-1}, which is in good agreement with the SFR calculated by Lunnan et al. (2014), Leloudas et al. (2015), and Schulze et al. (2018) and also

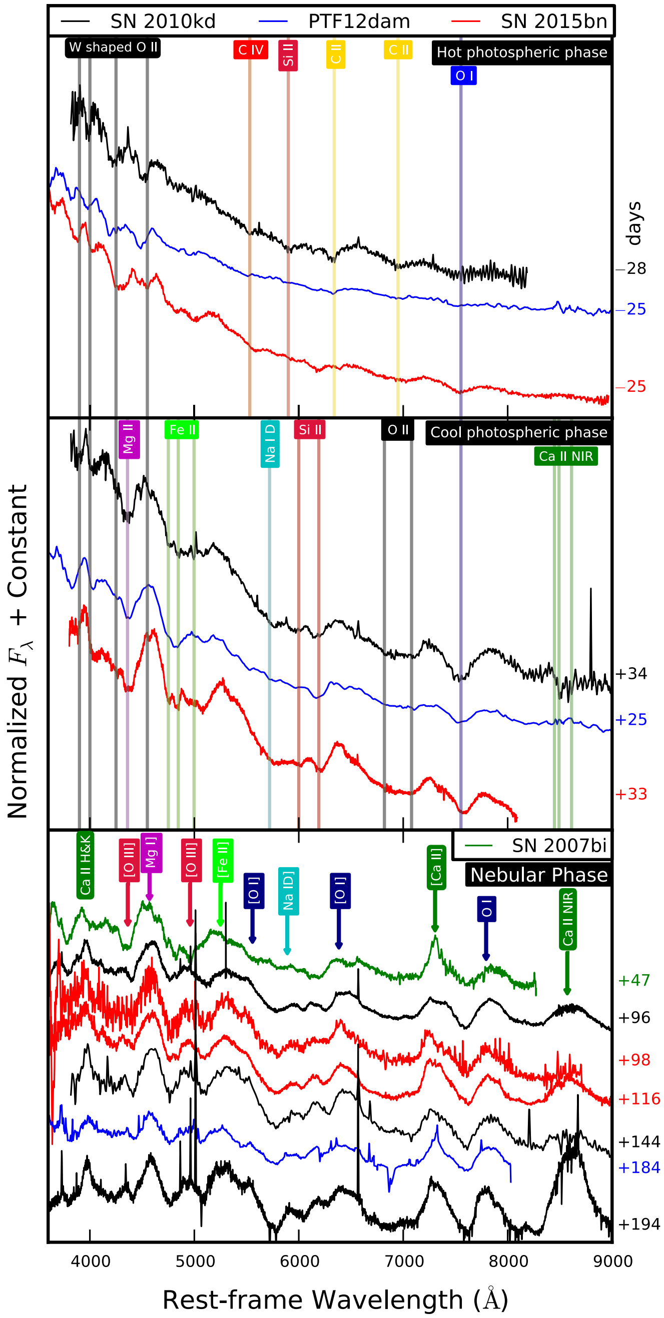

Figure 11. Spectra of SN 2010kd and three slow-decaying SLSNe I at possible similar phases are compared. Spectra of SN 2007bi are plotted in green, SN 2010kd in black, PTF12dam in blue, and SN 2015bn in red. The spectral evolution of SN 2010kd appears to be an excellent match to those of SN 2007bi, PTF12dam, and SN 2015bn in the photospheric as well as nebular phases.

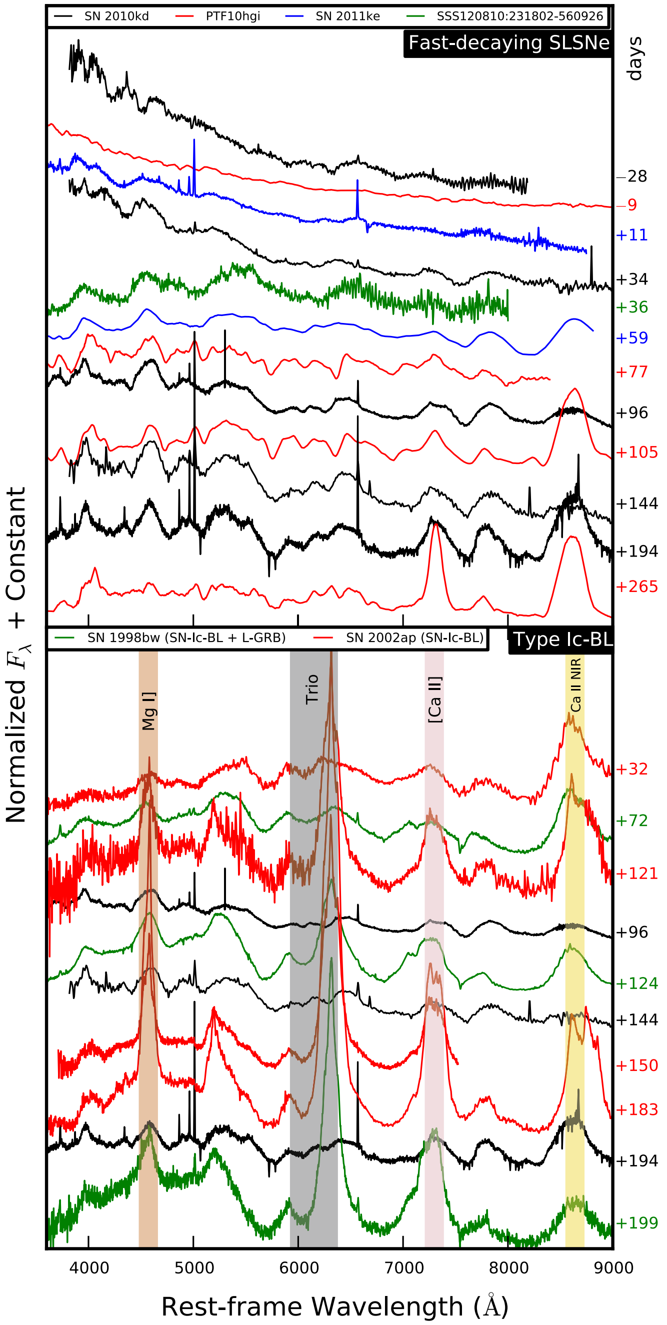

Figure 12. Upper: spectral comparison of SN 2010kd with three well-studied fast-decaying SLSNe I: PTF10hgi, SN 2011ke, and SSS120810:231802–560926. This comparison shows that fast-decaying SLSNe I spectroscopically evolve faster in comparison to SN 2010kd. Lower: comparison of late-phase spectra of SN 2010kd with two well-studied SNe Ic-BL: SN 1998bw and SN 2002ap. SN 2010kd and SNe Ic-BL seem to have many similar lines but with different intensities.

within the range of SFRs estimated for other well-studied SLSN hosts.

We also traced Hα, Hβ, Hγ, Hδ, [N II] λ6584, [O II] $\lambda\lambda$3726, 3729, [O III] λ4363, and [O III] $\lambda\lambda$4959, 5007 narrow host-galaxy emission lines in our nebular-phase spectra, particularly at +194 days (see Figure 8; narrow black arrows). These lines are similar to those observed by Lunnan et al. (2014) in late-time spectra of many SLSN hosts. In the case of SLSN iPTF13ehe, broad Hα and Hβ emission lines overlapping with narrow ones have been explained in terms of H-rich CSM at larger radii during late nebular phases (Yan et al. 2015, 2017b). The absence of broad Hα and Hβ emission lines in the nebular-phase spectra of SN 2010kd at +194 days excludes the possibility of late-time interaction of the SN envelope with H-rich material.

Observed narrow emission lines from the host are contaminated by the SN contribution itself; thus, their fluxes and lower limits of their equivalent widths (EWs) were estimated using a single-Gaussian fit (see Table 9). The measured flux values are generally higher than those of Lunnan et al. (2014),

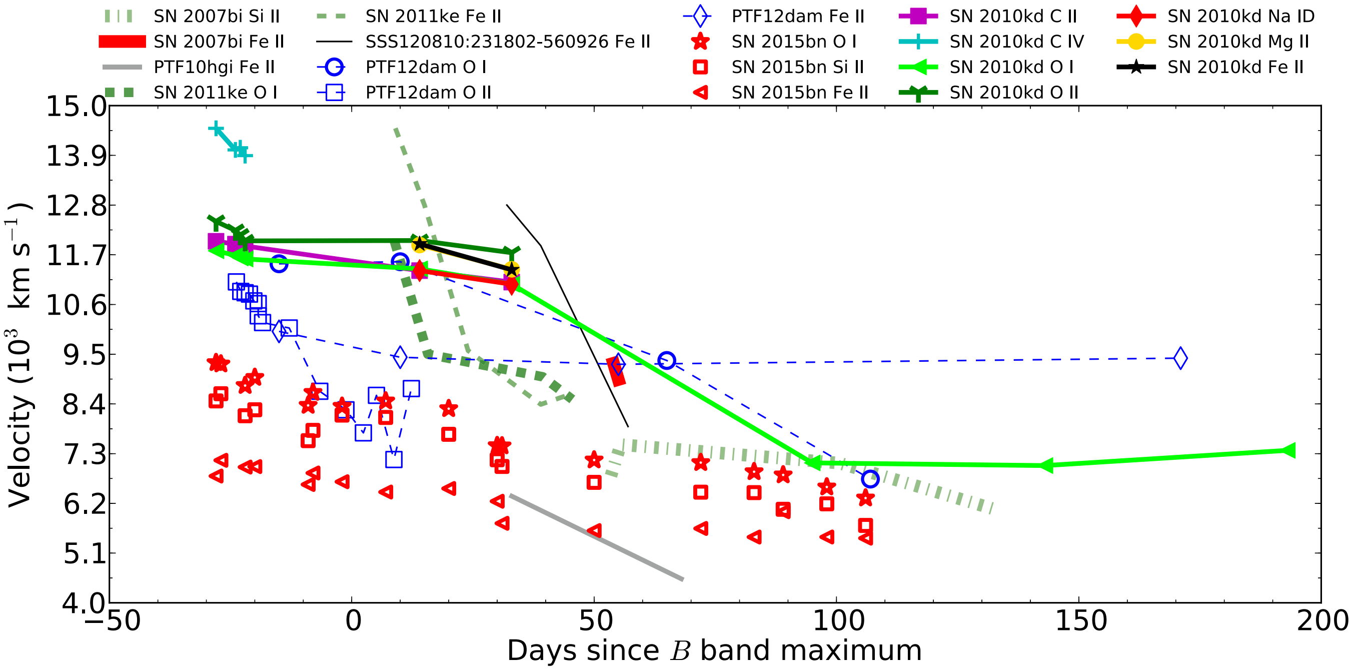

Figure 13. Line velocities of SN 2010kd are compared with a set of well-studied SLSNe I at comparable redshift. Measurements were made by `SYNAPPS` spectral matching; owing to blending of different elements, the single-Gaussian-fitting method is not a good way to calculate velocities. In comparison to SN 2010kd, fast-decaying SLSNe as well as PTF12dam appear to have velocities with steeper decay rates, whereas SN 2015bn seems to have lower velocity values with similar decay rates. Data Sources: Young et al. (2010), Inserra et al. (2013), Nicholl et al. (2016b), Liu et al. (2017), Quimby et al. (2018).

perhaps owing to a larger slit width or worse seeing. As discussed, in the present study we estimated the lower limit of EW[O III] ∼17.85 Å. However, Leloudas et al. (2015) estimated the upper limit of EW[O III] ∼190 Å, which placed the host galaxy of SN 2010kd in the category of extreme emission-line galaxies. The derived ratios of [O III]/Hβ and [N II]/Hα using the line fluxes (see Table 9) indicate that the host galaxy of SN 2010kd could be a low-luminosity, high-SFR dwarf galaxy having extreme emission lines as concluded by Leloudas et al. (2015).

9. Summary of Results

We have presented a detailed study of the photometric and the spectroscopic evolution of SN 2010kd, one of the closest slow-decaying SLSNe I. Using ROTSE-IIIb discovery data and other multiband data obtained using *Swift*-UVOT and the literature, we constructed a densely sampled optical light curve. Spectroscopy is presented from −28 to +194 days, obtained using the HET-9.2 m and Keck-10m telescopes. The temporal and spectral evolution of SN 2010kd is found similar to those of slow-decaying SLSNe I: SN 2007bi, PTF12dam, and SN 2015bn. A summary of the other major findings of our present analysis is as follows:

1. The *B*-band light curve of SN 2010kd has a peak luminosity close to that of PTF12dam and Gaia16apd, but higher in comparison to fast-decaying SLSNe I at comparable redshifts. Its postpeak decay rate is similar to that of SN 2007bi, PTF12dam, and SN 2015bn (slow decliners), and shallower than those exhibited by PTF10hgi, SN 2011ke, and SSS120810:231802–560926 (fast decliners).
2. The ($U-B$) color evolution of SN 2010kd shows that at phases from ∼+15 to +90 days, it is brighter in the *U* band and gets redder faster in the *U* than in the *B*, *V*, *R*, and *I* bands. This may be because of the cooling due to expansion or enhancement of the metallic lines in the UV or a combination of these two.
3. Analytic light-curve model fitting to the bolometric light curve of SN 2010kd using the code `Minim` suggests that CSMI/MAG may be possible powering sources for SN 2010kd.
4. The SED of the SN 2010kd matches a hot BB in the optical bands. In the photospheric phase, the continuum temperature of SN 2010kd looks somewhat hotter in comparison with PTF12dam and SN 2015bn. However, SN 2010kd seems to have a smaller BB radius in comparison to SN 2015bn.
5. During the photospheric phase, the spectra of SN 2010kd are dominated by the O I, O II, C II, C IV, and Si II lines; however, they are overcome by heavy metallic lines in the cool photospheric phase. Low- and high-velocity components of O II and Si II lines in the postmaximum spectra suggest possible nuclear burning fronts in the outer layers of the ejecta.
6. Early and late-time spectral comparisons of SN 2010kd reveal that it is similar to SN 2007bi, PTF12dam, and SN 2015bn with minor discrepancies. At ∼+96 days, SN 2010kd has spectra similar to those of fast-decaying SLSNe I at ∼+35 days, indicating a comparatively higher ejected mass of SN 2010kd.
7. A systematic comparison of the late-time spectra of SN 2010kd with those of broad-lined SNe Ic and those associated with LGRBs reveals that they have similar lines with different intensities, possibly providing clues to the variations in physical conditions among these events.
8. SN 2010kd exhibit relatively flatter line-velocity curves, similar to those of SN 2015bn, but at comparatively higher values. The velocity of the Fe II λ5169 line at

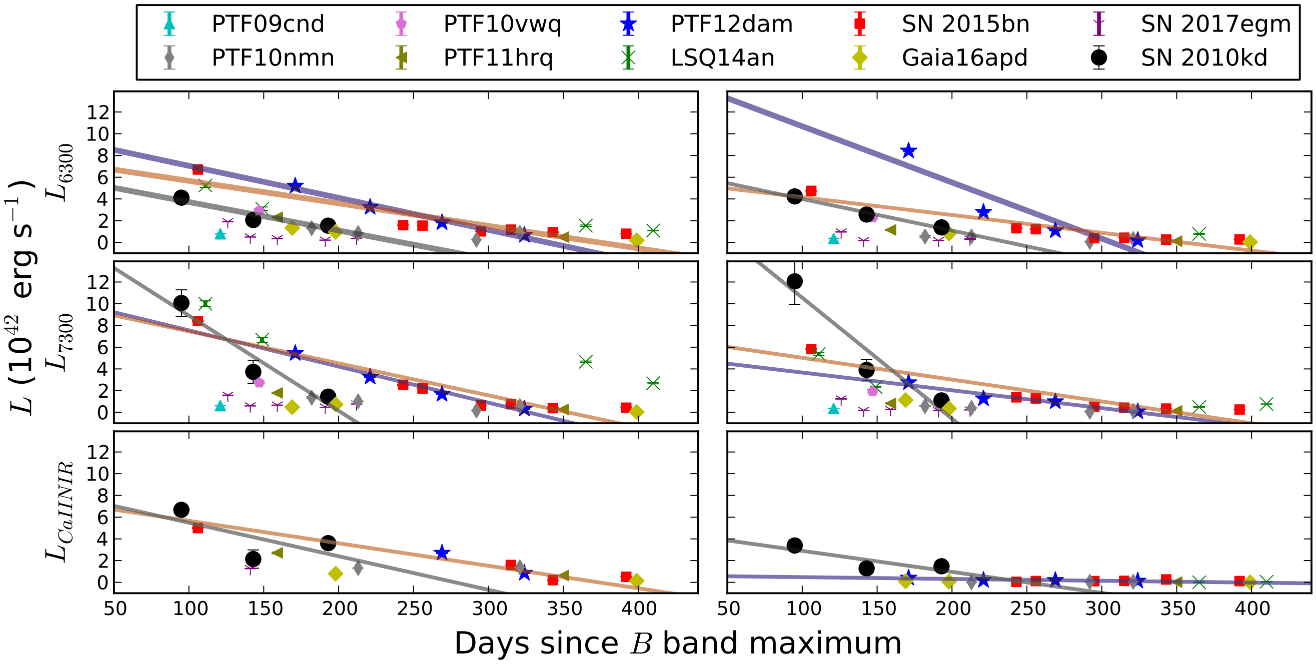

Figure 14. Integrated emission-line luminosities of SN 2010kd compared with a set of well-studied SLSNe I published in the literature. Line luminosities of SN 2010kd (in black), PTF12dam (in blue), and SN 2015bn (in red) are fitted with straight lines (as shown with respective colors) to make a rough estimate of line luminosities and line-luminosity decay rates. Most of the line luminosities of SN 2010kd seem to have higher values at +96 days as well as higher luminosity decay rates than other SLSNe I. By comparing the [O I] $\lambda\lambda$6300, 6364 line luminosity of SN 2010kd with that of other SLSNe I, we estimated an upper limit of O I ejected mass of ∼10 $M_\odot$. Data sources: Nicholl et al. (2013, 2016a, 2016b, 2017, 2019), Chen et al. (2015), Inserra et al. (2017), Jerkstrand et al. (2017), Kangas et al. (2017), Quimby et al. (2018).

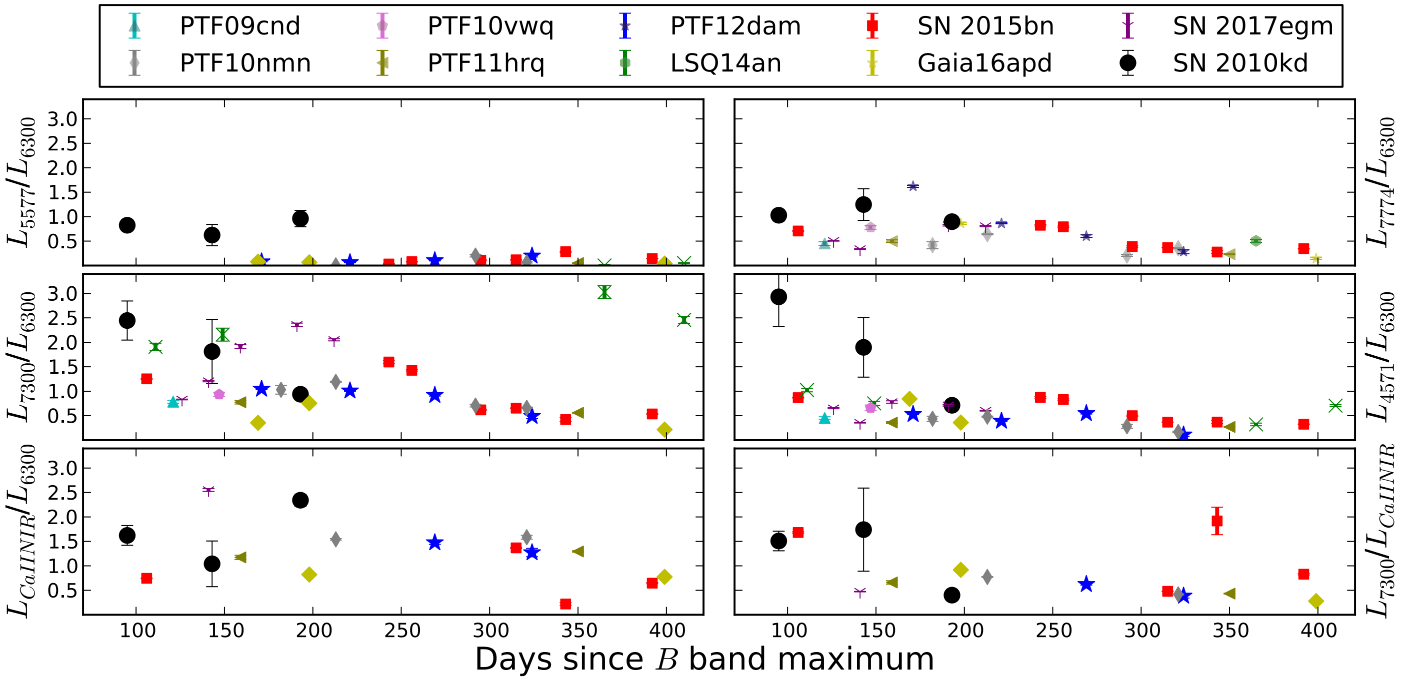

Figure 15. Line-luminosity ratios of SN 2010kd are compared with well-studied SLSNe I. [O I] λ5577, O I λ7774, Mg I], [Ca II], and the Ca II NIR triplet luminosities are normalized to the luminosity of [O I] $\lambda\lambda$6300, 6364. The [Ca II] line luminosity is normalized also with the Ca II NIR triplet. For SN 2010kd, L_{5577}/L_{6300} is higher than other presented SLSNe I, which indicates a higher single-zone LTE temperature (∼6000 K).

∼+10 days and its slow-decay rate up to ∼+30 days placed SN 2010kd in the category of slow decliners. The flatter line-velocity curves of SN 2010kd indicates a central engine power source.

(9) In the nebular-phase spectra of SN 2010kd, the Mg I] emission line has the highest luminosity of $\sim 10^{42}$ erg s^{-1} at +96 days, dropping to $\sim 10^{40}$ erg s^{-1} at +194 days. All of the emission lines show an overall decay in luminosity as phase increases.

(10) In comparison to other SLSNe I, SN 2010kd shows a higher luminosity ratio of [O I] λ5577 to [O I] $\lambda\lambda$6300, 6364 emission lines, indicating a higher single-zone LTE

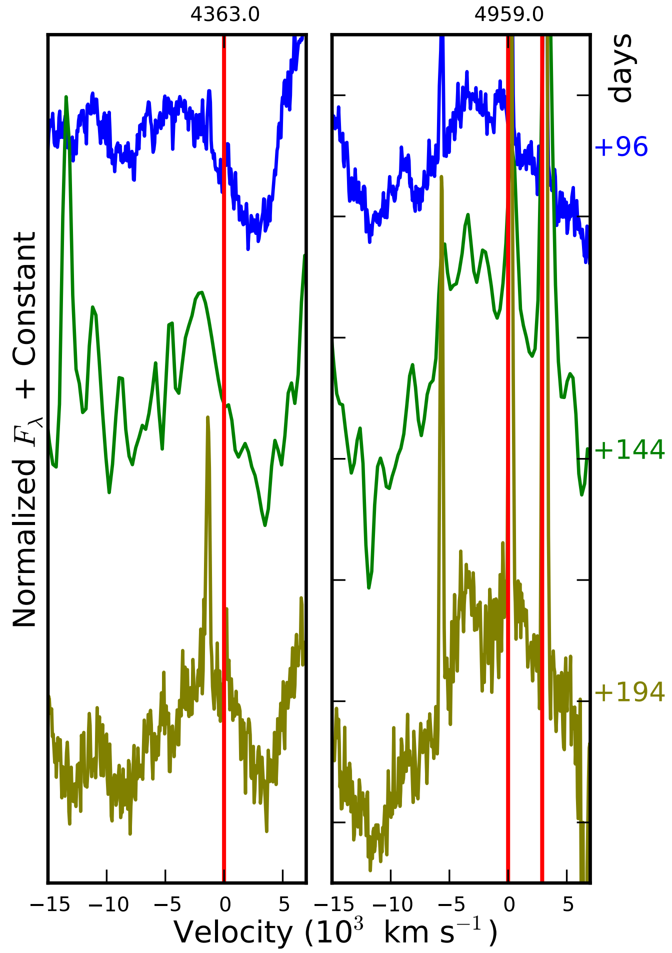

Figure 16. Evolution of the broad [O III] emission line of SN 2010kd at +96, +144, and +194 days. Left: evolution of [O III] λ4363; zero velocity is set at 4363 Å. Right: evolution of [O III] λλ4959, 5007; zero velocity is set at 4959 Å. At +96 days, the [O III] lines of SN 2010kd show $f_{4959,\,5007}/f_{4363} \approx 1.6$; at $T \approx 8000$ K; this corresponds to an electron density of $\sim 6.0 \times 10^7$ cm^{-3}.

Table 8

$L_{5577}/L_{6300,6364}$ and LTE Temperature[a]

Time (days)	$\frac{L_{5577}}{L_{6300,6364}}$ ($\beta_{\rm ratio} = 1.5$)	LTE T (K)
+96	0.80 ± 0.10	6090 ± 190
+144	0.60 ± 0.25	5700 ± 440
+194	0.95 ± 0.30	6320 ± 520

Note.

[a] The line-luminosity ratio $L_{5577}/L_{6300,6364}$ and the single-zone LTE temperature corresponding to this ratio. For all line-luminosity measurements, we choose $\beta_{\rm ratio} = 1.5$ as estimated by Jerkstrand et al. (2014).

temperature of SN 2010kd (∼6000 K). However, the lower line luminosity of [O I] λλ6300, 6364 in comparison to [Ca II] λ7300 indicates a central engine power source. Comparison of the [O I] λλ6300, 6364 line luminosity with that of other SLSNe I suggests an upper limit of O I ejected mass of $\sim 10\,M_\odot$ for SN 2010kd.

(11) The nebular spectra of SN 2010kd show a broad component of the [O III] λ4363 and λλ4959, 5007 lines that suggests the electron density of the emitting medium to be $\sim 6.0 \times 10^7$ cm^{-3}. These features are comparatively weaker in the spectra of PTF12dam.

Table 9

List of Host-galaxy Emission Lines of SN 2010kd

Line	Flux (10^{-16} erg s^{-1} cm^{-2})	EW (lower limit) (Å)
Hα	5.67 ± 0.24	16.20 ± 0.71
Hβ	1.86 ± 0.27	3.9 ± 0.56
Hγ	1.02 ± 0.25	1.91 ± 0.47
Hδ	0.45 ± 0.25	0.85 ± 0.48
[N II] λ6584	0.06 ± 0.4	0.19 ± 1.28
[O II] λ3727	2.39 ± 0.45	4.54 ± 0.86
[O III]λ4363	0.17 ± 0.15	0.33 ± 0.28
[O III]λ4959	2.97 ± 0.26	5.48 ± 0.48
[O III]λ5007	8.87 ± 0.36	17.78 ± 0.73

(12) The SFR ($\sim 0.18 \pm 0.04\,M_\odot$ yr^{-1}) for the host galaxy of SN 2010kd is constrained using the rest-frame UV flux. The derived flux ratios of [O III]/Hβ and [N II]/Hα are in agreement with previous findings, suggesting that the host of SN 2010kd is a low-luminosity, high-SFR dwarf galaxy.

This paper includes data taken from the RSVP program of the ROTSE-IIIb telescope (supported by NASA grant NNX10A196H, PI Carl Akerlof) at the McDonald Observatory of The University of Texas at Austin, 9.2 m HET, and 10.0 m Keck telescopes.

The HET is a joint project of the University of Texas at Austin, the Pennsylvania State University, Stanford University, Ludwig-Maximilians-Universität München, and Georg-August-Universität Göttingen. Some of the data presented herein were obtained at the W. M. Keck Observatory, which is operated as a scientific partnership among the California Institute of Technology, the University of California, and NASA. This work also uses data supplied by the UK *Swift* Science Data Centre at the University of Leicester and *Swift*-UVOT data released in the *Swift* Optical/Ultraviolet Supernova Archive (SOUSA). S.B.P., K.M., D.B., A.A., and R.G. acknowledge BRICS grant DST/IMRCD/BRICS/Pilotcall/ProFCheap/2017(G) and DST/JSPS grant DST/INT/JSPS/P/281/2018 for this work. J.V. and R.K-T. are supported by the project "Transient Astrophysical Objects" GINOP 2.3.2-15-2016-00033 of the National Research, Development, and Innovation Office (NKFIH), Hungary, funded by the European Union. The research of J.C.W. is supported in part by NSF AST-1813825. A.V.F.'s supernova group is grateful for the support of the TABASGO Foundation, the Christopher Redlich Fund, and the Miller Institute for Basic Research in Science (U.C. Berkeley). A.K. is grateful to Dr. Matt Nicholl for sharing the ASCII file from the published data. A.K. also acknowledges the PhD thesis of Rupak Roy as reference for some of the published photometric data taken with the 1.04 m Sampurnanand Telescope of ARIES Nainital. A.K. and team members are grateful to the referee for constructive comments that improved the manuscript. This research has utilized the NED, which is operated by the Jet Propulsion Laboratory, California Institute of Technology, under contract with NASA. We acknowledge the availability of NASA ADS services. This research also made use of the Open Supernova Catalog (OSC) currently maintained by James Guillochon and Jerod Parrent.

Facilities: HET-9.2 m, Keck:I, *Swift*.

Software: Python, matplotlib (Hunter 2007), HEASOFT (HEASARC 2014), *IRAF* (Tody 1986, 1993), ximage (v4.5.1), `sms` (Inserra et al. 2018c), `Superbol` (Nicholl 2018), `Minim` (Chatzopoulos et al. 2013), `SYNAPPS` (Thomas et al. 2011).

Appendix A

Optical, Swift-UVOT, and Swift-XRT Data Reduction of SN 2010kd

A.1 Optical Data Analysis

Reduction of ROTSE-IIIb data is discussed in Section 2.2. Published optical photometry in the Johnson *UBV* and Cousins *RI* bands is taken from Roy (2012). The *B*- and *R*-band photometry also estimated from spectra using the code `sms` (Inserra et al. 2018c).

A.2. Swift-*UVOT Data Analysis*

We analyzed all of the publicly available early-time (Target ID 00031890, 2010) and late-time (Target ID 00085565, 2014–2016) observations of *Swift*-UVOT. As part of the present analysis, UVOT data were obtained from the online archive[19] and analyzed using HEASOFT software v. 6.25 with the latest calibration database. We perform the reduction of the early-time UVOT data using the standard uvotproduct pipeline. A source circular region of 5″ and background region of 50″ radius were extracted for analysis. All of the estimated magnitudes in different filters are given in Tables 10 and 11.

UVOT again started following SN 2010kd during 2014–2016 in the *u* filter. In search of the host galaxy, all late-time sky images (Target ID 00085565) were stacked after their alignment to perform photometry of the source using the uvotsource pipeline (if visible after stacking or their upper limits). We summed the extensions within a sky image using uvotimsum. To sum the sky images from different observations, we merged the images first, using fappend. We considered the background threshold to be equal to three for calculating the magnitude of the source using uvotsource. A very faint extended object was detected, probably the host galaxy of SN 2010kd. Table 11 shows the filter, start time $t_{\rm start}$, and stop time $t_{\rm stop}$ (relative to the trigger time), total exposure time, magnitude, and significance of the source in *u* for the late-time observations. There is no correction for the Galactic extinction of the magnitudes given in Tables 10 and 11.

Table 10
Swift-UVOT Photometry of SN 2010kd

Filter	MJD	Magnitude	Obs ID
u	55,530.19	16.46 ± 0.04	00031890001
u	55,530.93	16.31 ± 0.07	00031890002
u	55,546.31	16.11 ± 0.03	00031890003
u	55,549.06	16.14 ± 0.03	00031890004
u	55,552.39	16.22 ± 0.03	00031890005
u	55,555.82	16.29 ± 0.03	00031890006
b	55,530.19	17.47 ± 0.05	00031890001
b	55,546.31	17.13 ± 0.03	00031890003
b	55,549.06	17.15 ± 0.05	00031890004
b	55,552.39	17.14 ± 0.03	00031890005
b	55,555.82	17.20 ± 0.04	00031890006
v	55,530.18	17.21 ± 0.07	00031890001
v	55,530.91	17.11 ± 0.05	00031890002
v	55,546.30	17.01 ± 0.05	00031890003
v	55,549.05	17.07 ± 0.05	00031890004
v	55,552.39	16.97 ± 0.04	00031890005
v	55,555.81	17.01 ± 0.05	00031890006
uvw1	55,530.18	17.35 ± 0.07	00031890001
uvw1	55,530.92	16.97 ± 0.05	00031890002
uvw1	55,546.30	16.81 ± 0.04	00031890003
uvw1	55,549.06	16.90 ± 0.05	00031890004
uvw1	55,552.39	16.99 ± 0.04	00031890005
uvw1	55,555.82	17.11 ± 0.05	00031890006
uvw2	55,530.18	18.69 ± 0.15	00031890001
uvw2	55,530.91	18.30 ± 0.09	00031890002
uvw2	55,546.30	17.95 ± 0.07	00031890003
uvw2	55,549.05	17.96 ± 0.07	00031890004
uvw2	55,552.39	18.13 ± 0.07	00031890005
uvw2	55,555.81	18.22 ± 0.08	00031890006
uvm2	55,530.18	18.14 ± 0.14	00031890001
uvm2	55,530.92	17.65 ± 0.09	00031890002
uvm2	55,546.30	17.51 ± 0.07	00031890003
uvm2	55,549.05	17.47 ± 0.07	00031890004
uvm2	55,552.39	17.59 ± 0.07	00031890005
uvm2	55,555.81	17.70 ± 0.08	00031890006

A.3. Swift-*XRT Data Analysis*

The *Swift*-XRT also observed the field of SN 2010kd. We analyzed all of the early-time XRT observation at the position of SN 2010kd. For this purpose, XRT data were obtained from the online archive[20] and analyzed using HEASOFT software v. 6.25 with the latest calibration database. We cleaned all of the XRT data using xrtpipeline, which removes the effects of hot pixels and Earth brightness. The ximage tool was used to detect the source, but no X-ray source was detected in individual images or in the stacked image near the UVOT position.

We coadded all individual observations (Obs IDs) using the ximage software package (v. 4.5.1) to produce a sky image of SN 2010kd. We then used the sosta pipeline to determine the significance of the source's count-rate upper limit in individual Obs IDs as well as in the stacked image. These count rates were converted to an unabsorbed flux in Table 12 using the online pimms tool (v. 4.9) using the appropriate column density for the host galaxy (Kalberla et al. 2005) and adopting a power-law spectral model with photon index $\Gamma = 2$. We converted unabsorbed flux into the luminosity using luminosity–distance information. We found that the unabsorbed flux and X-ray luminosity of each Obs Id are typically similar to those estimated by Levan et al. (2013) and Margutti et al. (2018).

---

[19] http://swift.gsfc.nasa.gov/docs/swift/archive/

[20] https://www.swift.ac.uk/xrt_products/index.php

Table 11
Host-galaxy Magnitudes from Stacked Late-time *Swift*-UVOT Images

Filter	t_{start} (s) MJD = 56,980.90	t_{stop} (s) MJD = 57,561.00	Exp. (s)	Magnitude (mag)	Significance
u	4.381254199412E+08	4.882461009676E+08	16,792.18	21.54 ± 0.23	4.7σ

Table 12
Log of *Swift*-XRT Upper Limits on Unabsorbed Flux, 0.3–10 keV Band

UT Date	MJD	Obs ID	Exposure (s)	Unabsorbed Flux (0.3–10 keV) (10^{-14} erg s^{-1} cm^{-2})	L_X (10^{42} erg s^{-1})
2010 Nov 30	55530.13	00031890001	1785	$<$23.96	$<$5.2
2010 Nov 30	55530.91	00031890002	1788	$<$32.73	$<$8.6
2010 Dec 16	55546.29	00031890003	3181	$<$13.49	$<$3.5
2010 Dec 19	55549.04	00031890004	2811	$<$14.88	$<$3.9
2010 Dec 22	55552.38	00031890005	3476	$<$12.17	$<$3.2
2010 Dec 25	55555.81	00031890006	3428	$<$12.13	$<$34.2
Stacked	Stacked	Stacked	16,472	$<$3.096	$<$0.8

Appendix B
`SYNAPPS` Spectral Matching

The best-fit parameters obtained from `SYNAPPS` spectral matching to the photospheric-phase spectra of SN 2010kd (see Figure 6) are listed in Table 13. These parameters are the line opacity τ, lower and upper cutoff velocities v_{min} and v_{max} (respectively), e-folding length aux, and BB photospheric temperature T. It uses the aux parameter for deciding the form of opacity and the Boltzmann excitation temperature for line-strength parameterization. The YAML[21] file consists of a few more parameters known as coefficients of the quadratic warping function, which is multiplied by the synthetic spectrum after proper computation. The limitations of this code are a sharp photosphere, BB assumption, and the approximation of no electron scattering.

---

[21] See http://www.yaml.org.

Table 13
Best-fit Parameters Obtained Using `SYNAPPS` Spectral Matching

Element	log τ	$v_{\rm min}$ (10^3 km s^{-1})	$v_{\rm max}$ (10^3 km s^{-1})	aux	T (10^3 K)
At −28 days					
C II	−1.25	12.0	41.14	12.0	15.32
C IV	−0.54	14.5	20.44	6.97	18.43
O I	0.4	11.79	30.0	1.45	19.23
O II	−0.28	12.44	29.92	0.42	17.11
Si II	0.23	21.99	40.85	5.5	6.01
Fe III	−0.27	11.8	30.87	1.58	16.72
At −24 days					
C II	−1.02	11.94	41.53	4.99	14.31
C IV	−0.61	14.02	22.37	6.33	25.0
O I	0.42	11.69	30.0	1.4	19.03
O II	−0.5	12.24	29.93	0.42	17.08
Si II	−0.66	13.26	44.91	10.0	11.86
Fe III	−1.51	11.71	29.9	2.1	5.0
At −23 days					
C II	−1.18	11.85	40.59	5.69	13.48
C IV	−0.58	14.07	24.12	6.17	25.0
O I	0.4	11.63	30.0	1.38	18.83
O II	−1.36	12.14	29.93	0.42	19.44
Si II	−0.75	13.48	40.31	10.0	10.56
Fe III	−0.36	11.7	29.87	1.81	14.79
At −22 days					
C II	−1.31	11.89	34.58	10.0	14.26
C IV	−0.73	13.89	21.25	10.0	22.99
O I	0.39	11.61	30.0	1.43	18.23
O II	−0.53	12.01	29.93	0.42	16.66
Si II	−0.29	22.75	38.46	9.44	7.08
Fe III	−1.25	11.64	26.58	12.0	9.98
At +15 days					
C II	−1.43	11.35	49.42	3.29	11.03
O I	0.17	11.39	49.97	1.96	5.6
O II LV	−0.47	12.02	49.93	3.15	11.1
O II HV	−0.63	21.5	49.91	14.99	11.1
Na I	−0.64	11.35	49.89	5.47	19.88
Mg II	−0.25	11.92	49.92	2.83	13.23
Si II LV	−0.03	11.35	49.84	2.92	17.13
Si II HV	−0.13	19.0	49.97	8.36	17.13
Fe II	−0.67	11.94	49.37	5.64	8.22
At +34 days					
C II	−1.92	11.1	49.88	10.0	12.86
O I	0.17	11.05	49.93	1.98	5.83
O II LV	−0.63	11.75	49.43	5.29	11.08
O II HV	−0.64	19.52	49.95	15.0	11.08
Na I	−0.37	11.05	49.9	2.8	5.21
Mg II	−0.34	11.38	49.91	2.85	20.0
Si II LV	−0.05	11.05	49.92	2.57	17.49
Si II HV	−0.11	18.73	39.78	8.73	17.49
Fe II	−0.64	11.36	42.75	9.81	10.35

ORCID iDs

Amit Kumar https://orcid.org/0000-0002-4870-9436
Jozsef Vinko https://orcid.org/0000-0001-8764-7832
WeiKang Zheng https://orcid.org/0000-0002-2636-6508
Alexei V. Filippenko https://orcid.org/0000-0003-3460-0103
Robert Kehoe https://orcid.org/0000-0002-7101-697X
Robert Quimby https://orcid.org/0000-0001-9171-5236
Emmanouil Chatzopoulos https://orcid.org/0000-0002-8179-1654
Raya Dastidar https://orcid.org/0000-0001-6191-7160
Anjasha Gangopadhyay https://orcid.org/0000-0002-3884-5637
Kuntal Misra https://orcid.org/0000-0003-1637-267X
Brajesh Kumar https://orcid.org/0000-0001-7225-2475

References

Akerlof, C. W., Kehoe, R., McKay, T., et al. 2003, PASP, 115, 132
Angus, C. R. 2017, PhD thesis, Univ. Warwick, http://wrap.warwick.ac.uk/95533/
Angus, C. R., Smith, M., Sullivan, M., et al. 2019, MNRAS, 487, 2215
Bessell, M. S. 1990, PASP, 102, 1181
Bianco, F. B., Modjaz, M., Hicken, M., et al. 2014, ApJS, 213, 19
Bose, S., Dong, S., Pastorello, A., et al. 2018, ApJ, 853, 57
Brachetti, P., de Felice Ciccoli, M., di Pillo, G., et al. 1997, J. Global Optimization, 10, 165
Chatzopoulos, E., Wheeler, J. C., & Vinko, J. 2012, ApJ, 746, 121
Chatzopoulos, E., Wheeler, J. C., Vinko, J., et al. 2013, ApJ, 773, 76
Chen, J., Wang, X., Ganeshalingam, M., et al. 2014, ApJ, 790, 120
Chen, T.-W., Nicholl, M., Smartt, S. J., et al. 2017a, A&A, 602, 9
Chen, T.-W., Smartt, S. J., Bresolin, F., et al. 2013, ApJL, 763, L28
Chen, T.-W., Smartt, S. J., Jerkstrand, A., et al. 2015, MNRAS, 452, 1567
Chen, T.-W., Smartt, S. J., Yates, R. M., et al. 2017b, MNRAS, 470, 3566
Chevalier, R. A., & Irwin, C. M. 2011, ApJL, 729, L6
Chornock, R., Berger, E., Rest, A., et al. 2013, ApJ, 767, 162
Cohen, M., Wheaton, W. A., & Megeath, S. T. 2003, AJ, 126, 1090
De Cia, A., Gal-Yam, A., Rubin, A., et al. 2018, ApJ, 860, 100
Dessart, L. 2019, A&A, 621, A141
Dessart, L., Hillier, D. J., Waldman, R., et al. 2012, MNRAS, 426, L76
Dhungana, G., Kehoe, R., Vinko, J., et al. 2016, ApJ, 822, 6
Fukugita, M., Ichikawa, T., Gunn, J. E., et al. 1996, AJ, 111, 1748
Gal-Yam, A. 2012, Sci, 337, 927
Gal-Yam, A. 2019, ARA&A, 57, 305
Gal-Yam, A., Mazzali, P., Ofek, E. O., et al. 2009, Natur, 462, 624
Hatano, K., Branch, David., Fisher, A., et al. 1999, ApJ, 525, 881
Hill, G. J., Nicklas, H. E., MacQueen, P. J., et al. 1998, Proc. SPIE, 3355, 433
Hogg, D. W., Baldry, I. K., Blanton, M. R., et al. 2002, arXiv:astro-ph/0210394
Hunter, J. D. 2007, CSE, 9, 90
Inserra, C. 2019, NatAs, 3, 697
Inserra, C., Nicholl, M., Chen, T.-W., et al. 2017, MNRAS, 468, 4642
Inserra, C., Nicholl, R. C., Scovacricchi, D., et al. 2018a, A&A, 609, A83
Inserra, C., Prajs, S., Gutierrez, C. P., et al. 2018b, ApJ, 854, 175
Inserra, C., Smartt, S., Jerkstrand, A., et al. 2013, ApJ, 770, 128
Inserra, C., Smartt, S. J., Gall, E. E. E., et al. 2018c, MNRAS, 475, 1046
Jeffery, D. J., & Branch, D. 1990, in Supernovae, ed. J. C. Wheeler, T. Piran, & S. Weinberg (Singapore: World Scientific), 149
Jerkstrand, A., Smartt, S. J., Fraser, M., et al. 2014, MNRAS, 439, 3694
Jerkstrand, A., Smartt, S. J., Inserra, C., et al. 2017, ApJ, 835, 13
Jordi, K., Grebel, E. K., & Ammon, K. 2006, A&A, 460, 339
Kalberla, P. M. W., Burton, W. B., Hartmann, D., et al. 2005, A& A, 440, 775
Kangas, T., Blagorodnova, N., Mattila, S., et al. 2017, MNRAS, 469, 1246
Kasen, D., & Bildsten, L. 2010, ApJ, 717, 245
Kasen, D., Woosley, S. E., & Heger, A. 2011, ApJ, 734, 102
Kennicutt, R. C., Jr. 1998, ARA&A, 36, 189
Leloudas, G., Schulze, S., Krühler, T., et al. 2015, MNRAS, 449, 917
Levan, A. J., Read, A., Metzger, B., et al. 2013, ApJ, 771, 136
Liu, Yu-Q., Modjaz, M., & Bianco, F. B. 2017, ApJ, 845, 85
Lunnan, R., Chornock, R., Berger, E., et al. 2014, ApJ, 787, 138
Lunnan, R., Chornock, R., Berger, E., et al. 2016, ApJ, 831, 144
Lunnan, R., Chornock, R., Berger, E., et al. 2018, ApJ, 852, 81
Margutti, R., Chornock, R., Metzger, B. D., et al. 2018, ApJ, 864, 45
Maurer, I., & Mazzali, P. A. 2010, MNRAS, 408, 947
Mazzali, P. A., Sullivan, M., Pian, E., et al. 2016, MNRAS, 458, 3455
McCrum, M., Smartt, S. J., Rest, A., et al. 2015, MNRAS, 448, 1206

Metzger, B. D., Giannios, D., Thompson, T. A., et al. 2011, MNRAS, 413, 2031

Moriya, T. J., Sorokina, E. I., & Chevalier, R. A. 2018, SSRv, 214, 59

Nasa High Energy Astrophysics Science Archive Research Center (HEASARC) 2014, HEASOFT: Unified Release of FTOOLS and XANADU, Astrophysics Source Code Library, ascl:1408.004

Neill, J. D., Sullivan, M., Gal-Yam, A., et al. 2011, ApJ, 727, 15

Nicholl, M. 2018, RNAAS, 2, 230

Nicholl, M., Berger, E., Blanchard, P. K., et al. 2019, ApJ, 871, 102

Nicholl, M., Berger, E., Margutti, R., et al. 2016a, ApJL, 828, L18

Nicholl, M., Berger, E., Margutti, R., et al. 2017, ApJL, 835, 8

Nicholl, M., Berger, E., Smartt, S. J., et al. 2016b, ApJ, 826, 39

Nicholl, M., Smartt, S. J., Jerkstrand, A., et al. 2013, Natur, 502, 346

Nicholl, M., Smartt, S. J., Jerkstrand, A., et al. 2014, MNRAS, 444, 2096

Nicholl, M., Smartt, S. J., Jerkstrand, A., et al. 2015a, MNRAS, 452, 3869

Nicholl, M., Smartt, S. J., Jerkstrand, A., et al. 2015b, ApJL, 807, 18

Oke, J. B., Cohen, J. G., Carr, M., et al. 1995, PASP, 107, 375

Osterbrock, D. E., & Ferland, G. J. 2006, Astrophysics of Gaseous Nebulae and Active Galactic Nuclei (2nd ed.; Sausalito, CA: University Science Books)

Pastorello, A., Smartt, S. J., Botticella, M. T., et al. 2010, ApJL, 724, L16

Perley, D. A., Quimby, R. M., Yan, L., et al. 2016, ApJ, 830, 13

Planck Collaboration XIII, Ade, P. A. R., Aghanim, N., et al. 2016, A&A, 594, 13

Poole, T. S., Breeveld, A. A., Page, M. J., et al. 2008, MNRAS, 383, 627

Prajs, S., Sullivan, M., Smith, M., et al. 2017, MNRAS, 464, 3568

Quimby, R. M., Aldering, G., Wheeler, J. C., et al. 2007, ApJL, 668, L99

Quimby, R. M., De Cia, A., Gal-Yam, A., et al. 2018, ApJ, 855, 2

Quimby, R. M., Kulkarni, S. R., Kasliwal, M. M., et al. 2011, Natur, 474, 487

Quimby, R. M., Yuan, F., Akerlof, C., et al. 2013, MNRAS, 431, 912

Roy, R. 2012, PhD Thesis, ARIES/Kumaun Univ.

Schlegel, D. J., Finkbeiner, D. P., & Davis, M. 1998, ApJ, 500, 525

Schulze, S., Krühler, T., Leloudas, G., et al. 2018, MNRAS, 473, 1258

Sollerman, J., Kozma, C., Fransson, C., et al. 2000, ApJ, 537, 127

Taddia, F., Stritzinger, M. D., Bersten, M., et al. 2018, A&A, 609, A136

Thomas, R. C., Nugent, P. E., & Meza, J. C. 2011, PASP, 123, 237

Tody, D. 1986, Proc. SPIE, 627, 733T

Tody, D. 1993, in ASP Conf. Ser. 52, Astronomical Data Analysis Software and Systems II, ed. R. J. Hanisch, R. J. V. Brissenden, & J. Barnes (San Francisco, CA: ASP), 173

Umeda, H., & Nomoto, K. 2008, ApJ, 673, 1014

Vinko, J., Blake, R. M., Sarneczky, K., et al. 2004, A&A, 427, 453

Vinko, J., Zheng, W., Pandey, S. B., et al. 2012, AAS Meeting 219, 436.04

Vinko, J., Zheng, W., Romadan, A., et al. 2010, CBET, 2556, 1

Wang, S., Wang, L., & Dai, Z. G. 2019, RAA, 19, 63

Wheeler, J. C., Chatzopoulos, E., Vinko, J., et al. 2017, ApJ, 851, 14

Wheeler, J. C., Johnson, V., & Clocchiatti, A. 2015, MNRAS, 450, 1295

Wheeler, J. C., Yi, I., Höflich, P., & Wang, L. 2000, ApJ, 537, 810

Woosley, S. E. 2010, ApJL, 719, L204

Yan, L., Lunnan, R., Perley, D. A., et al. 2017a, ApJ, 848, 6

Yan, L., Quimby, R., Gal-Yam, A., et al. 2017b, ApJ, 840, 57

Yan, L., Quimby, R., Ofek, E., et al. 2015, ApJ, 814, 108

Young, D., Smartt, S., Valenti, S., et al. 2010, A&A, 512, A70